REVIEW

National Science Open
2: 20220059, 2023
https://doi.org/10.1360/nso/20220059

Chemistry

Special Topic: Chemistry Boosts Carbon Neutrality

Recent advances in carbon-supported non-precious metal single-atom catalysts for energy conversion electrocatalysis

Li-Xia Liu[1,#], Yangyang Ding[1,#], Linan Zhu[2], Jin-Cheng Li[3], Huitong Du[1], Xiang Li[1], Zhaoyuan Lyu[2], Dan Du[2], Fuqiang Liu[1], Yuanyuan Wang[1,*], Wenlei Zhu[1,*] & Yuehe Lin[2,*]

[1]*State Key Laboratory of Pollution Control and Resource Reuse, State Key Laboratory of Analytical Chemistry for Life Science, the Frontiers Science Center for Critical Earth Material Cycling, School of the Environment, School of Chemistry and Chemical Engineering, Nanjing University, Nanjing 210023, China;*
[2]*School of Mechanical and Materials Engineering, Washington State University, Pullman WA 99164, USA;*
[3]*Faculty of Chemical Engineering, Yunnan Provincial Key Laboratory of Energy Saving in Phosphorus Chemical Engineering and New Phosphorus Materials, Kunming University of Science and Technology, Kunming 650500, China*

#Contributed equally to this work.
*Corresponding authors (emails: wangyy@nju.edu.cn (Yuanyuan Wang); wenleizhu@nju.edu.cn (Wenlei Zhu); yuehe.lin@wsu.edu (Yuehe Lin))

Received 17 September 2022; Revised 15 January 2023; Accepted 16 January 2023; Published online 27 February 2023

Abstract: Non-precious metal single-atom catalysts (NPM-SACs) with unique electronic structures and coordination environments have gained much attention in electrocatalysis owing to their low cost, high atomic utilization, and high performance. NPM-SACs on carbon support (NPM-SACs/CS) are promising because of the carbon substrate with a large surface area, excellent electrical conductivity, and high chemical stability. This review provides an overview of recent developments in NPM-SACs/CS for the electrocatalytic field. First, the state-of-the-art synthesis methods and advanced characterization techniques of NPM-SACs/CS are discussed in detail. Then, the structural adjustment strategy of NPM-SACs/CS for optimizing electrocatalytic performance is introduced concisely. Furthermore, we provide a comprehensive summary of recent advances in developing NPM-SACs/CS for important electrochemical reactions, including carbon dioxide reduction reaction, hydrogen evolution reaction, oxygen evolution reaction, oxygen reduction reaction, and nitrogen reduction reaction. In the end, the existing challenges and future opportunities of NPM-SACs/CS in the electrocatalytic field are highlighted.

Keywords: single-atom catalysts, non-precious metal, electrocatalytic reaction, carbon-supported

Introduction

The rapid consumption of traditional fossil fuels has led to a global energy crisis and environmental challenges, which has made the research on renewable energy conversion systems, such as fuel cells, and electrolyzers, becoming the current research hotspot [1–9]. Electrocatalysts play critical roles in the energy conversion reactions like carbon dioxide reduction reaction (CO_2RR) [10,11], hydrogen evolution reaction (HER) [12,13], oxygen evolution reaction (OER) [14–16], oxygen reduction reaction (ORR) [17–20], and nitrogen reduction reaction (NRR) [21–23]. Over the last few decades, many materials have been studied,

like noble metals, transition metals, and metal-free carbons to improve the performance of electrocatalysts. So far, heterogeneous catalysts have been extensively used in the current chemical industry process, but their low atom utilization efficiency often limits their catalytic performance. Beyond the heterogeneous catalysts, another type of catalysts, homogeneous molecular catalysts possess high atom utilization efficiency and convenient structural tunability. However, these catalysts are usually expensive, unstable, and not reusable [22,24]. Thus, developing novel catalysts with the advantages of both heterogeneous and homogeneous catalysts is necessary.

Single-atom catalysts (SACs), as a new type of catalyst, have attracted much attention owing to their multiple advantages, such as high metal atom utilization, high catalytic activity, and tunable metal-support interactions [25,26]. Different terms have been used to describe these atomically dispersed metal catalysts, such as single-site heterogeneous catalysts, atomically dispersed supported metal heterogeneous catalysts, or site-isolated heterogeneous catalysts and SACs. There are already excellent articles detailing the similarities and differences among these concepts [27,28]. In this review, we will use the term SACs, referring to the catalysts that only contain isolated single atoms dispersed on the surface of the support with no interaction among the isolated atoms.

In 2011, Zhang Tao's research group [29] successfully dispersed isolated Pt atoms on FeO_x and prepared SACs of Pt_1/FeO_x, which were used for CO oxidation and formally proposed the concept of single-atom catalysis. Since then, the field of single-atom catalysis has been booming [30–36]. In fact, before the concept of single-atom catalysis was put forward, relevant research on SACs had already appeared. In 1925, Taylor *et al*. [37] found that atoms with different saturation degrees would affect the catalytic capabilities. Subsequently, in 1964, chemisorption between the surface-isolated center of a metal catalyst and intermediates containing π bonds in hydrocarbon reactions was investigated [38]. In 1999, Iwasawa's research group [39] prepared atomic-level dispersion catalysts $PtMo_6$/MgO and Pt(A)/MgO by dispersing platinum atoms on the surface of MgO, and found that prepared atomic-level dispersion catalysts had a better catalytic activity of propane oxygenation than nano-catalysts. In 2003, the Flytzani-Stephanopoulos research group [40] studied the catalytic activity of atomically dispersed catalysts Pt/CeO_2 and Au/CeO_2 in the water-gas conversion reaction and also found that the performance of these atomically dispersed catalysts was better than that of nanoparticles. In 2005, Xu Baiqing's research group [41] successfully synthesized atomic-level dispersion Au/ZrO_2 catalyst and reported that the selective hydrogenation of 1,3-butadiene to produce butadiene has a 100% selectivity and a high conversion rate of 80%–90%. The isolated Au^{3+} ions in the catalyst showed high activity in the selective hydrogenation reaction, which further proved that the active center of the catalytic reaction was atomically dispersed metal ions. In 2007, Lee's group [42] prepared Pd/Al_2O_3 catalyst with a load mass fraction of 0.03% atomic-level dispersion and observed Pd single atoms loaded on the Al_2O_3 surface by using high-resolution spherical aberration electron microscopy. These early studies enabled researchers to have a deeper understanding of the isolated active sites of catalysts, and further provided inspiration and help for the subsequent research and the concept of single-atom catalysis.

In recent years, SACs have become the most popular and active research direction in the field of catalysis. Major breakthroughs have been made in previous research on the precise design, synthesis, characterization of SACs, the construction of new load materials, and the improvement of single-atom load [43]. In 2017, the Datye research group [44] prepared Pt/CeO_2 SAC by high-temperature pyrolysis of Pt nanoparticles and loading atomically dispersed Pt^{2+} on CeO_2, which successfully realized the low-temperature oxidation of CO.

This study provides a new idea for the preparation of SACs. In 2019, Lang *et al*. [35] prepared high-load Pt SAC with high-temperature resistance by means of the metal-carrier covalent strong interaction, aiming at the loading and stability of single atom, and made a breakthrough in improving the stability and loading of SACs. At the same time, a new method to obtain SACs with high stability and load was provided: simple impregnation followed by high-temperature roasting. In 2021, Gu *et al*. [45] made full use of the synergistic effect of metal-carrier interaction and space confined domain effect of SACs to obtain high reactivity and high stability of SACs. Different from traditional methods, this research group synthesized Ni_1Cu_2/g-C_3N_4 triatomic catalyst with high single-atom load through the synergistic effect of metal-carrier interaction and space limitation, which provided a new way for the design of highly active and stable SACs.

Due to the high surface energy of the single metal atom, they needed to be coordinated and stabilized by the substrates. Various materials have been explored as substrates for constructing SACs, including transition metal compounds [46–49], MXene [50–52], and carbon materials [53–57]. Thereinto, carbon substrates aroused broad concerns due to their outstanding conductivity and pore structure, which could accelerate the electron/mass transfer rate of the reactants/intermediates for promoting catalytic activity [58,59]. Furthermore, the structural tunability and designability of carbon materials, such as amorphous carbon, graphite, and diamond, make it possible to investigate their valuable structure-property correlations, which are essential for a deeper understanding of catalytic mechanisms and the design of high-performance catalysts [60]. In addition, the central metal atoms also play critical roles in the catalytic performance of SACs. In recent years, many metal atoms such as Ru, Pt, Fe, Co, Ni, Cu, and Zn, anchored on carbon-supported substrates have been developed for electrochemical reactions [61–67]. Compared to precious metal SACs, the advantages of non-precious metal SACs are very prepotent, such as low cost, abundant reserves, and more extensive sources, which accelerate large-scale commercial deployment in energy-related fields. Therefore, from a practical point of view, SACs composed of earth-abundant non-precious metals seem more attractive than expensive noble metal catalytic systems. Tremendous advances in non-precious metal SACs on carbon support (NPM-SACs/CS) for many energy-conversion reactions have been achieved, making it possible for NPM-SACs/CS to outcompete traditional metal particle catalysts in the renewable energy market [58,59]. Therefore, a comprehensive review of the NPM-SACs/CS specifically for energy conversion reactions is necessary.

In this review, we first summarize the advanced synthesis methods for preparing high-performance NPM-SACs/CS. Then, to reveal the structure of NPM-SACs/CS at atomic and electronic levels, state-of-the-art characterization techniques including experimental and theoretical technologies are comprehensively discussed. Furthermore, to better optimize the catalytic performance, the structure tuning strategy of NPM-SACs/CS is also introduced in this review paper. Afterward, the application of NPM-SACs/CS in electrochemical reactions is comprehensively summarized. These applications mainly involve CO_2RR, HER, OER, ORR, and NRR. Finally, the challenges and development opportunities of NPM-SACs/CS are a further prospect. And this review can provide necessary information for the rational design and synthesis of future NPM-SACs/CS.

Synthesis methods for NPM-SACs/CS

Generally, NPM-SACs/CS exhibit excellent catalytic activity for electrochemical reactions. However, during

the synthesis procedure, highly dispersed single atoms are prone to migration and agglomeration due to the higher surface energy. Thereby, exploring novel synthesis methods to prepare highly stable and highly loaded single-atom catalysts is critical. Here, the methods of high-temperature pyrolysis, physical and chemical deposition, impregnation adsorption, ball milling, and ultrafast synthesis for NPM-SACs/CS are summarized.

High-temperature pyrolysis

High-temperature pyrolysis is one of the most common means to prepare NPM-SACs/CS. In the atmosphere of inert gas (N_2, Ar) or reducing gas (NH_3, H_2), the reaction precursors containing non-precious metals (Cu, Fe, Co, and Ni) are carbonized after high-temperature calcination. After high-temperature treatment, the metal atoms exist in covalent bonds with the support, which significantly improves the stability and dispersion of single atoms. The design routes of pyrolysis mainly include but are not limited to *in situ* polymerization, carbon supports connection, metal-organic frameworks (MOFs) construction, and sacrificial template-assisted route.

In situ polymerization

In the self-polymerization or condensation process of some organic molecules with symmetric structures, metal precursors can be introduced and coordinated with multiple N-dentate ligands to form stable atomic-level dispersion, and then SACs are obtained by high-temperature pyrolysis. This method of *in situ* self-polymerization usually automatically carbonizes or graphitizes at high temperatures without the introduction of some carbon substrates, which simplifies the experimental process. Typically, Li's group [68] introduced a pyrrole-thiophene copolymer pyrolysis scheme to obtain Fe SACs based on sulfur and nitrogen co-doped carbon through high-temperature calcination (900°C). They also [69] synthesized Fe-N_4 SACs derived from bimetallic Zn/Fe polyphthalocyanine by a general polymerization-pyrolysis-evaporation strategy (Figure 1A), which is versatile in developing other single-atom metallic materials. Very recently, Lin's group [70] found that in addition to copolymers, single organometallic molecules $Na_2[Cu(EDTA)]•2H_2O$ could partially carbonize to N, O-coordinated Cu SACs at a gentle pyrolysis temperature (250°C). Compared with high-temperature pyrolysis, gentle pyrolysis shows higher research value, but it is trapped in the composition analysis dilemma caused by the unpredictable degree of carbonization.

Carbon supports connection

This is a method of combining metal precursors with some carbon materials, including N-doped carbon nanotubes (CNTs), carbon nitride (CN), graphene oxide (GO), carbon black, etc., by high-temperature calcination, which directly utilizes the bonding effect of the specific intermediate (N, O, S) on metal and carbon atoms. Because of the flexible coordination and stable bonding ability of many metal atoms, the N atom becomes the main choice for stabilizing the central metal atoms which may come either from the nitrogenous metal precursor or from the protective gas (NH_3) of the calcination process. Up to now, many NPM-SACs/CS have been prepared by this method, like the Fe SACs by pyrolysis of hemin on N-doped

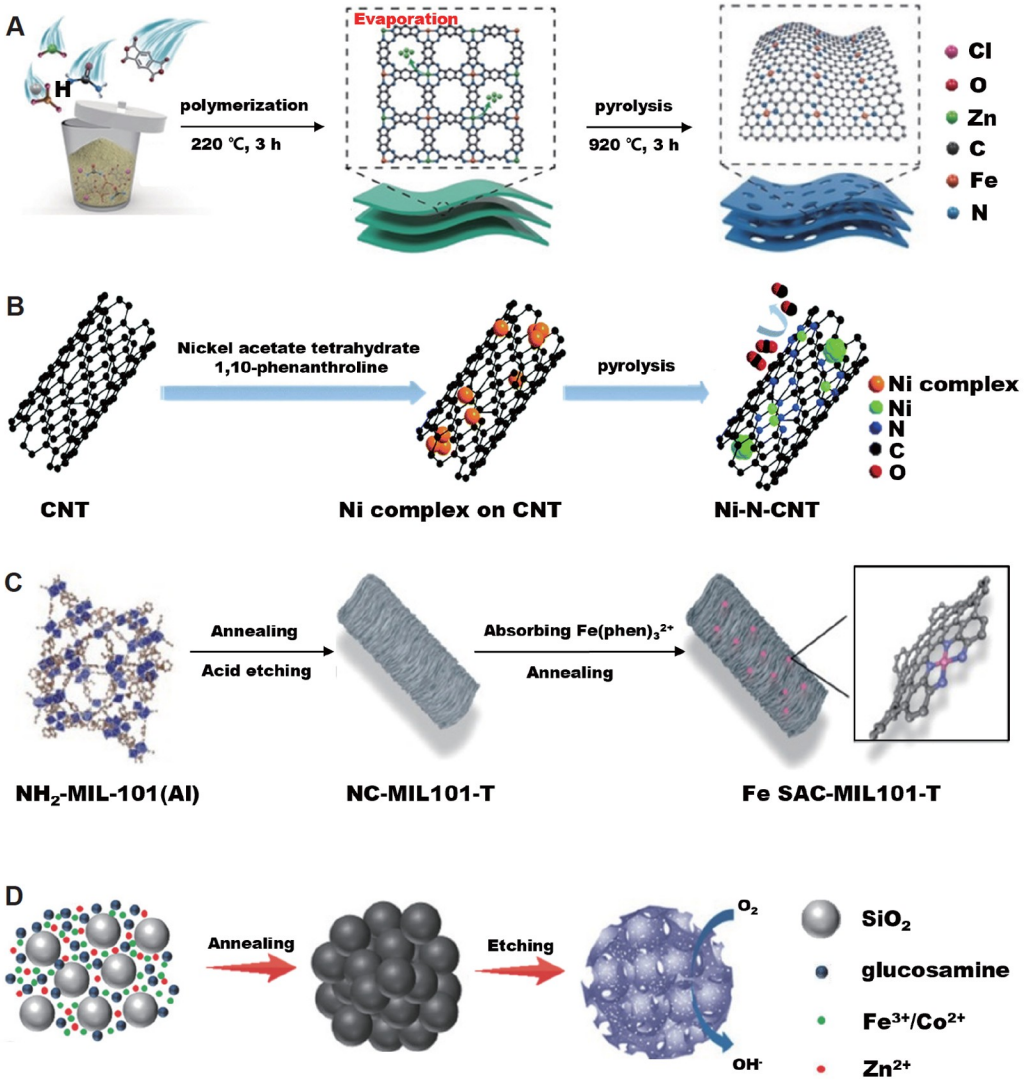

Figure 1 Representative carbon-based non-noble metal single-atom materials through different pyrolysis routes. (A) Preparation of Fe-N_4 SAC through support-free carbonization route. Reproduced with permission from ref. [69]. Copyright©2018, John Wiley and Sons. (B) Preparation of Ni-N-CNT catalyst through carbon supports connection route. Reproduced with permission from ref. [73]. Copyright©2021, Royal Society of Chemistry. (C) Preparation of Fe SAC-MIL 101-T through metal-organic frameworks (MOFs) construction route. Reproduced with permission from ref. [77]. Copyright©2021, John Wiley and Sons. (D) Preparation of Co, Fe-N-C mesoporous nanospheres SAC through sacrificial template-assisted route. Reproduced with permission from ref. [78]. Copyright©2018, John Wiley and Sons.

hierarchically porous carbon under Ar atmosphere [71], Ni SACs by pyrolysis of Ni (II) acetate and the Schiff base ligand (or phenanthroline) on carbon black (or CNTs) under Ar atmosphere (Figure 1B) [72,73], and Ni SACs by pyrolysis of the freeze-dried graphene impregnated with Ni^{2+} ions under NH_3 atmosphere [74].

MOF construction

The introduction of MOFs and their derivatives with porous effects and large specific surface area is an

important idea to improve the catalytic activity of carbon-based materials. Notably, sacrificial metal is necessary for the pyrolysis of bimetallic MOF precursors, such as the sacrificial metal Zn for ZIF-8 and Mg for MgNi-MOF-74, of which the existence promotes better dispersion of the host single atom. Lin and coworkers [75] synthesized Fe-doped ZIF-8 using 2-metholimidazole as the ligand reagent and further pyrolyzed it to obtain Fe SACs. Yang and coworkers [76] obtained Fe-N-C by brief high-temperature calcination after ball milling operation of Cd-Fe-DABCO-TPA MOF precursor and 1,10-phenanthroline. Impressively, Zhang and coworkers [77] reported support for single-metal MOF derivative (NC-MIL101-T), which was converted from NH_2-MIL-101(Al) MOF carried by air calcination and acid etching, and then converted to Fe SAC-MIL101-T by pyrolysis after adsorbing $Fe(phen)_3^{2+}$ precursor (Figure 1C).

Sacrificial template-assisted route

This is a new synthetic route that has developed rapidly in recent years. The pyrolysis of precursors on the template surface could bring specific morphologies, highly dispersed single atom sites, a unique mesoporous structure, and a huge specific surface area form in the wake of recovery of the template, thus facilitating the design of materials with versatile morphologies. For example, Zhu *et al*. [78] reported Co, Fe-N-C mesoporous nanosphere SACs through the bimodal template approach (Figure 1D), where silica colloid as sacrificial templates removed by hydrofluoric acid after pyrolysis, and glucosamine as the Co or Fe precursor. Yet, other mature sacrificial templates, such as $Mg(OH)_2$ template removed by HCl for preparing M-N-C (M = Co, Fe, Ni) moieties, a NaCl template removed by H_2O for preparing CoN_x [79–81] and FeN_3S have also been developed and applied continuously [82,83].

Physical and chemical deposition

SACs can be formed by deposing metal atoms onto selected carbon-based supports, e.g., atomic layer deposition (ALD) and chemical vapor deposition (CVD), and electrochemical deposition (ECD).

ALD is a method of alternately exposing the support material to the pulse vapor of different reaction precursors to make the substrate well-deposit layer by layer on the surface of the support in the form of a monatomic film. ALD can be traced back to the synthesis of polycrystalline fluorescent materials and amorphous insulating films. Since then, the ALD technique has been further developed in the synthesis of catalyst support materials, especially carbon-based catalysts containing precious metals [84–86], but in recent years, significant progress has also been made in non-precious metal-based materials. Generally, the regulation of morphology and quality of nanocrystals can be precisely controlled by simply adjusting the cycle number of ALD. For instance, by regulating the ALD cycle numbers, Lu and coworkers [87] successfully deposited Co ligand on reduced graphene oxide (GO) to obtain Co_1/G SACs through several ALD cycles accompanied by elevated temperature ozone treatment (Figure 2A). Similarly, Yao and coworkers [88] constructed the Co_1-N_4 SACs on phosphatized C_3N_4. It is worth noting that the ALD method still faces some opportunities and challenges in the design of NPM-SACs/CS. For instance, other non-precious metal centers such as Fe, Ni, and Cu have been rarely reported so far in this way; and the materials prepared by the ALD method are usually nonuniform in size and shape, resulting in a challenge to further study of the structure-activity relationship between material structure and catalytic properties [89].

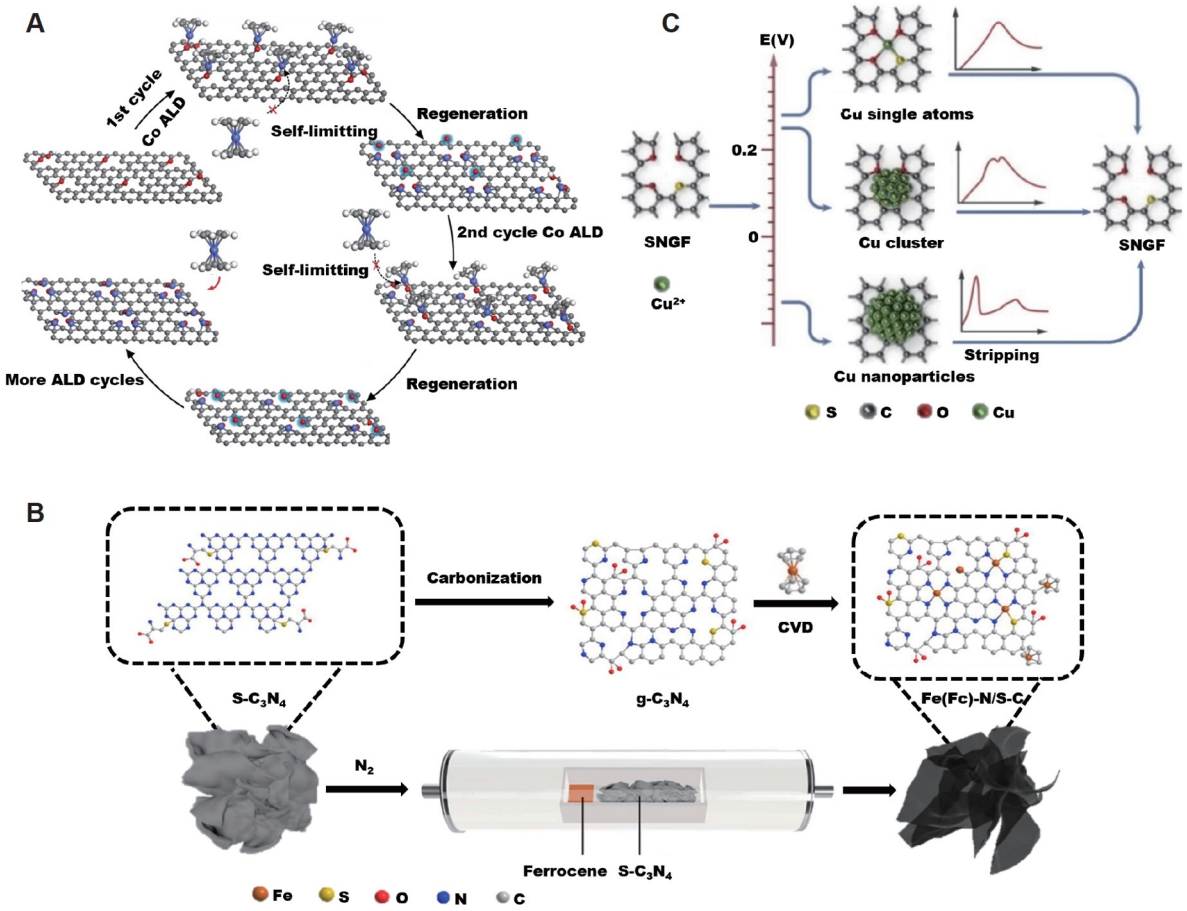

Figure 2 Representative non-noble metal SACs are supported on carbon materials by different deposition methods. (A) Co_1/G SACs synthesized by ALD. The blue, brown, red, and white balls represent Co, C, O, and H atoms, respectively. Reproduced with permission from ref. [87]. Copyright©2018, Springer Nature. (B) Fe-N/S-C structure synthesized by CVD. Reproduced with permission from ref. [91]. Copyright©2021, American Chemical Society. (C) Cu-SNGF SACs synthesized by ECD. Reproduced with permission from ref. [93]. Copyright©2021, Elsevier.

CVD is a material surface modification technology that endows the material surface with some special properties without changing the composition and weakening the strength of the matrix material. Chen's group [90] reported a 3D nanoporous graphene doped with both N and Ni single atoms/clusters, where the Ni doping amount and stability were significantly improved by the pre-doping of N using the chemical vapor deposition (CVD) method. Wu's group [91] found that the atomically dispersed single Fe sites could be inserted into the N, S co-doped 2D carbon nanosheets to establish Fe-N/S-C structure by taking the cyclopentadiene-shielded Fe atom ferrocene as a precursor (Figure 2B). Additionally, Ye's group [92] designed a low-temperature (450°C) CVD route to obtain Ni-NC@Ni core-shell nanostructure with Single-Ni sites.

ECD is a method of depositing metal precursors onto the support to form corresponding metal catalysts with the assistance of an applied electric field. Xu *et al*. [93] synthesized the Cu-SNGF SACs by using a low-potential deposition method to modify Cu SACs onto the nitrogen-doped graphite foam electrode (Figure 2C). Moreover, according to the study of Yang *et al*. [94], the metal immersed in the C_3N_4 suspension exhibited a high state near the negative electrode and consequently deposited onto the C_3N_4 under the action

of the electric field, and the results show that both noble and non-noble metal atoms (Ag, Cu, Ni, Co, V, Fe, Zn, Ru, Ce, Sm, Mo, W, Bi) can be well dispersed on the C_3N_4 support. The advantages of easy operation and high yield endow ECD with the strong ability of rapid and efficient preparation of SACs, however, the choice of carbon-based supports is limited, which needs to be further explored.

Impregnation adsorption

The adsorption of metal precursors dispersed in the liquid phase by the open carrier is the key to the preparation of SACs by the impregnation absorption method. This adsorption is weak and easy to dissociate, so subsequent steps such as freeze-drying and pyrolysis are needed to strengthen the fixation of single atoms. In addition, in order to form a highly dispersed single atom, the concentration of the precursor in the dispersed phase should not be too high, which in turn reduces the load of the single atom. For carbon-based materials, increasing the adsorption site and enhancing the adsorption are two important ways to improve the load of a single atom. For instance, Guo and colleagues [95] constructed a uniform arrangement of carbonized ZIF on nanofibers by using electrospinning technology, which significantly increased the specific surface area and the corresponding adsorption sites of the material combined ZIF with electrospun nanofiber through impregnation growth, and then the absorbed metal (Co and Ni) ion in ZIF *in situ* transformed to Co and Ni SACs with high load by subsequent pyrolysis treatment (Figure 3A). Furthermore, Lin and colleagues [96] demonstrated a high-loading Ce-N-C SACs involving well-designed support of special surfactant cetyltrimethylammonium bromide (CTAB) template-induced polypyrrole nanowire (Figure 3B), where the introduction of CTAB is beneficial to improve the absorption of Ce precursor at the defect site. More impressively, with the development of impregnation absorption technology, it is possible to synthesize NPM-SACs/CS in large quantities. Lu and colleagues [97] came up with an automated synthesis protocol to synthesize mono- or multimetallic SACs of more than 15 transition metals on different carbon-based supports, e.g., nitrogen-doped carbon and polymeric C_3N_4 (Figure 3C).

Ball milling

The merits of wide applications, small solvent consumption, and low pollution make ball milling as one of the most promising methods to prepare SACs in large quantities, while it is still restricted by the harsh operating conditions (for example, under 99.999% argon) and special precursors. Ball milling is generally used as a pretreatment to enhance the close contact between the solid precursor and the substrate as well as promote the overall dispersion of the two, which usually combines with pyrolysis or other subsequent operations to obtain SACs with high dispersion. Metal precursors can be derived from the metal-doped substrate or single metal powder, for example, the conversion of Fe-doped C_3N_4 and CNTs to Fe-N-CNT by ball milling and pyrolysis (Figure 4A) [98] and the conversion of the mixture of metal (Fe, Co, Ni) powder and NSC support (pyrolysis products of melamine and thioacetamide) to M-N_4-S (M = Fe, Co, Ni) structure by ball milling with acid washing (Figure 4B) [99]. Recent studies showed that SACs can be prepared by a simple one-step ball milling. Yang *et al*. [100] ground the zirconium dioxide capsules containing metal (i.e., Fe, Co, and Fe/Co) polyphthalocyanines and H_2O for 1 h, followed by centrifugation (3000 r/min for 30 min) of the resulting mixture to obtain the corresponding SACs (Figure 4C).

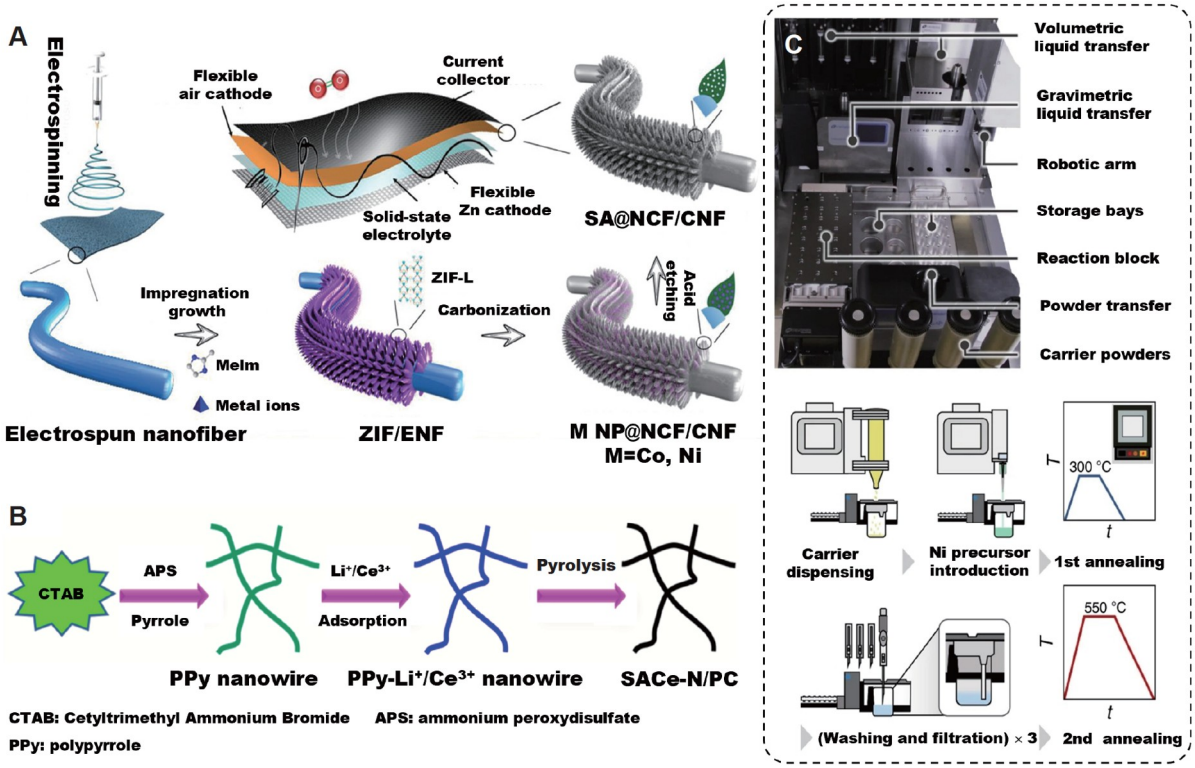

Figure 3 Representative NPM-SACs/CS are supported by carbon materials by the impregnation adsorption method. (A) M NP@NCF/CNF (M = Co, Ni) was obtained by impregnation growth, carbonization, and acid etching. Reproduced with permission from ref. [95]. Copyright©2019, John Wiley and Sons. (B) SACs-N/PC was obtained by impregnation, absorption, and pyrolysis. Reproduced with permission from ref. [96]. Copyright©2021, American Chemical Society. (C) Ni SACs with automated production. Reproduced with permission from ref. [97]. Copyright©2022, Springer Nature.

Photochemical route

The preparation of SACs by photochemical route is a green and simple method. The prerequisite of the photoreduction route is light irradiation which prompts the reduction of metal precursor into metal atoms. Metal precursor mainly includes metal salt or acid ion, which can be dissolved slowly after liquid freeze-drying for liquid phase photoreduction or adsorbed to the carrier by immersion method for solid phase photoreduction. Among them, liquid phase photoreduction reduces the diffusion rate and local reactant concentration by means of ultra-low temperature to inhibit the nucleation effect of metal atoms, thus increasing the nucleation barrier and ensuring high dispersion. While the formation of single-atom sites by solid-phase photoreduction focuses on the impregnation and adsorption of the substrate to the solution. Moreover, the control of low temperature should be highlighted in liquid phase photoreduction, and fluctuations in temperature may induce the formation of clusters or nanoparticles, while solid phase photoreduction relies little on temperature.

It is worth noting that the commonly used ultraviolet light source only shows a certain effect on the reduction of noble metal ions, such as Pt and Pd [101,102], which is rarely suitable for the preparation of non-noble metal SACs. The photo-induced reduction can be completely replaced by more powerful chemical reduction to enable the preparation of NPM-SACs/CS. The substitution process mostly exists in liquid-phase

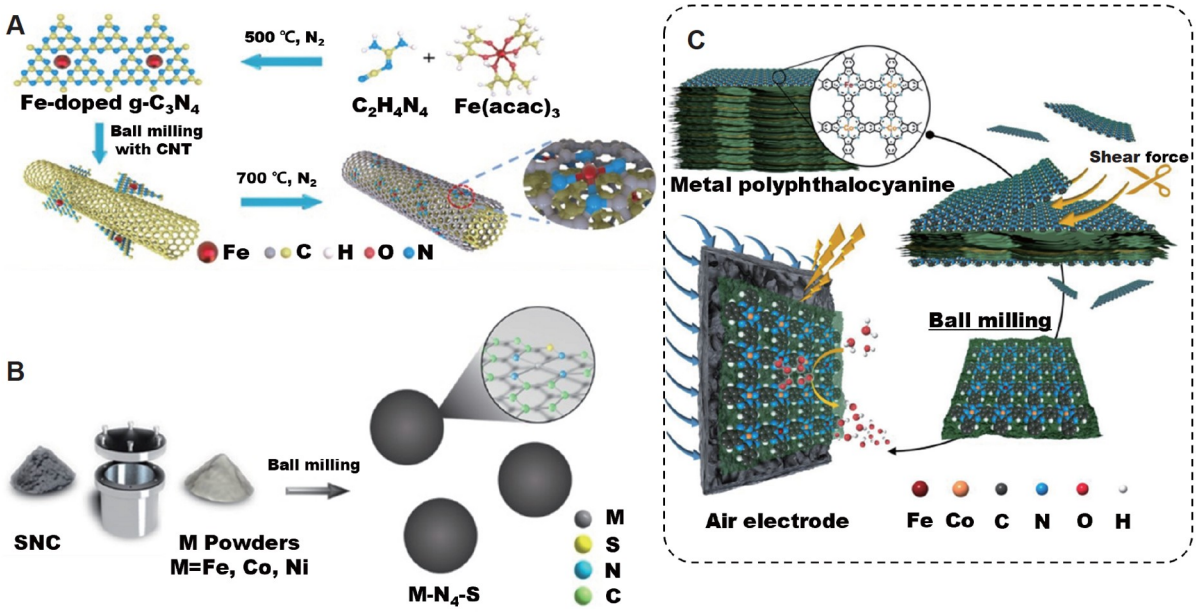

Figure 4 Representative non-noble metal SACs are supported on carbon materials by the ball milling method. (A) Fe-N-CNT is synthesized by ball milling and pyrolysis. Reproduced with permission from ref. [98]. Copyright©2021, American Chemical Society. (B) M-N_4-S (M = Fe, Co, Ni) structure synthesized by ball milling (with acid washing). Reproduced with permission from ref. [99]. Copyright©2021, John Wiley and Sons. (C) Fe, Co SACs synthesized by one-step ball milling. Reproduced with permission from ref. [100]. Copyright©2019, John Wiley and Sons.

photoreduction to liquid-phase chemical reduction. Wu and coworkers [103] rapidly freeze-dried a variety of metal salt solutions and then transferred them to the solution containing a strong reducing agent. Under the presence and carbon base, the metal salt ice melted naturally and slowly released with vigorous stirring at 0°C, preventing the nucleation process, and finally reduced the corresponding metal SACs (Figure 5A). They also found that noble metal (Ag, Au Rh, Ru, Pd, Ir, Pt, and Os) ions can be reduced in $NaBH_4$ solution, while non-noble metal (Ni, Co, Cu) ions require a more reducing environment (N_2H_5OH with KOH solution) to be reduced. In addition to being replaced by chemical reduction, it can also be replaced by photoexcited radical reduction. Most recently, Wang and coworkers [104] proposed a hydrogen-assisted photochemical strategy at room temperature to generate stable high-loaded SACs (Cu, Co) with non-strongly coordinated M-P_3 structures on two-dimensional (2D) black phosphorus (BP) supports. The formation of hydrogen radical (H) on the BP layer induced by visible light is the key to the preparation of high-loaded copper single atoms with metal atom loading up to 11.3% (Figure 5B).

Top-down atom-trapping strategy

A top-down atom-trapping strategy is defined by gasification of metal precursors through pyrolysis or atomic thermal migration at high temperatures, and then being captured by defective carbon substrates to form single atoms with stable dispersion and clear structure. The metal precursors that satisfy this method mainly include metal nanoparticles (Ag, Pt, Pd, and Ni nanoparticles) [34,105] or their elemental materials (Cu, Ni, Co foams, and Fe film) [95,106], metal oxides (Cu_2O, NiO, Fe_2O_3, MoO_3, Co_2O_3, SnO_2, and SrO) [107,108], metal salts ($CoCl_2$, H_2PtCl_6, H_2PdCl_4, $HAuCl_4$, and H_2IrCl_6) [109,110], which are able to release metal atoms

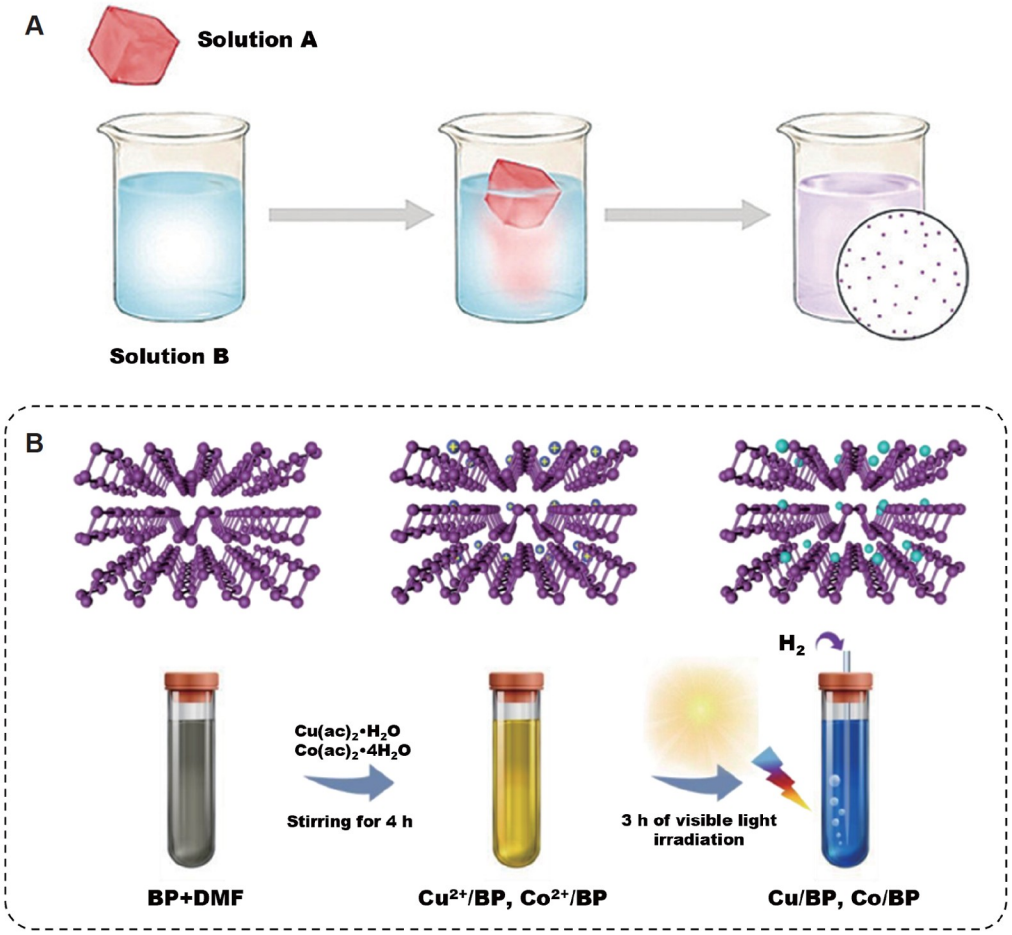

Figure 5 Representative non-noble metal SACs by the photochemical route. (A) Scheme of the synthesis of atomically dispersed metal single atoms. Solution A represents a metal salt solution and solution B represents a reducing solution. Reproduced with permission from ref. [103]. Copyright©2018, John Wiley and Sons. (B) Cu/BP and Co/BP structure synthesized by photoexcited radical reduction. Reproduced with permission from ref. [104]. Copyright©2022, Springer Nature.

well at high temperatures. In the process of preparing Ni SACs from Ni nanoparticles, the Ni nanoparticles were adsorbed to the defective N-containing carbon substrate (carbonized ZIF-8) by impregnation and absorption, then the mixture was ground to strengthen the particle dispersion, and finally, the highly dispersed Ni SACs were formed by calcination at high temperature (Figure 6A) [105]. In contrast, the preparation of Cu SACs from Cu_2O mainly relied on high temperature to promote the formation of volatiles of Cu_2O, which migrated to the defects of carbonized ZIF-8, and then be reduced to Cu single atoms (Figure 6B) [109]. $CoCl_2$ can also thermally migrate to ultrathin N-rich carbon substrates at high temperatures and directly obtain the corresponding Co SACs (Figure 6C) [109]. Compared with the metal oxide route, the metal salt route avoids introducing corrosive reducing gases (NH_3), making it simpler and more environmentally friendly.

Ultrafast synthesis

In addition to the widely used methods mentioned above, some other methods reported recently have been

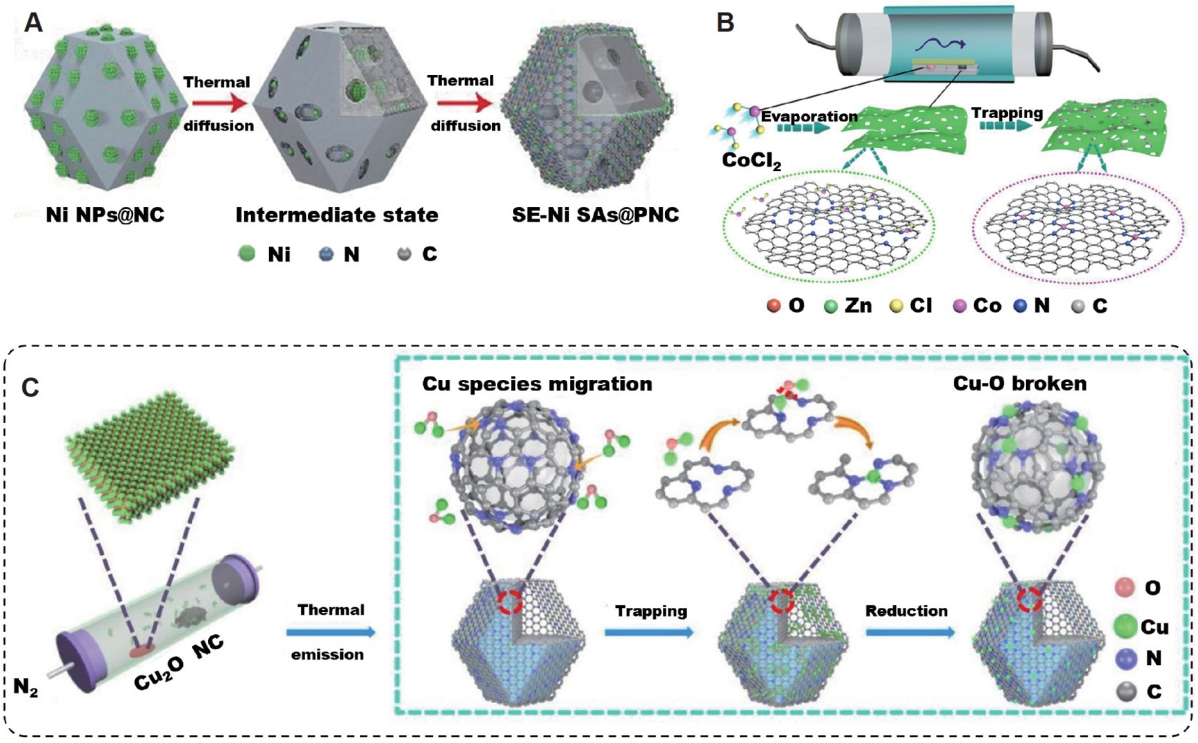

Figure 6 Representative non-noble metal SACs are supported on carbon materials by top-down atom-trapping strategy. (A) Synthesis of Ni SACs from Ni NPs [105]. Copyright©2018, John Wiley and Sons. (B) Synthesis of Cu SACs from Cu_2O with atom-trapping and reduction. Reproduced with permission from ref. [107]. Copyright©2019, Springer Nature. (C) Synthesis of Co SACs from $CoCl_2$ with atom-trapping. Reproduced with permission from ref. [109]. Copyright©2020, Springer Nature.

conceived to design NPM-SACs/CS, such as some ultrafast synthesis strategies under extreme heating conditions [111]. Ultrafast synthesis utilizes the high energy released during rapid ignition heating and instantaneous quenching processes such as current heating, microwave heating, laser radiation, and arc discharge. This method can promote the interaction of metal precursors with carbon-based supports at high energies. Thus, the high free energy of single-atom self-aggregation is overcome. Finally, the metal atoms' high dispersion and high loading are realized. Single atoms of various metal centers have been achieved in this way, such as the synthesis of Ni-N-C moieties supported on carbon black by current heating (Figure 7A) [112], single atomic transition metals (Co, Ni, Cu) embedded in nitrogen-doped graphene by two-second microwave heating (Figure 7B) [113], Co-P SACs based on highly conductive multiwall CNTs by pulsed laser confinement (PLC) operation (Figure 7C) [114], mono-dispersed Mn, Fe, Co, and Ni atom trapped in the crystalline carbon lattice of N-doped graphene by arc discharge (Figure 7D) [115]. Ultrafast synthesis has a unique advantage in the research and development of monatomic materials due to the high utilization of energy and time, which provides a new idea for the large-scale production of NPM-SACs/CS. Unfortunately, it is difficult to accurately detect the temperature in the rapid heating process, which brings certain difficulties to the synthesis and optimization of materials to further improve the load of metal atoms. In addition, rapid heating may cause overheating damage to the structure of materials, leading to synthesis failure. Therefore, rapid monitoring and accurate control of reaction temperature play a vital role in realizing ultrafast synthesis, which requires scholars to strive with perspiration and blood.

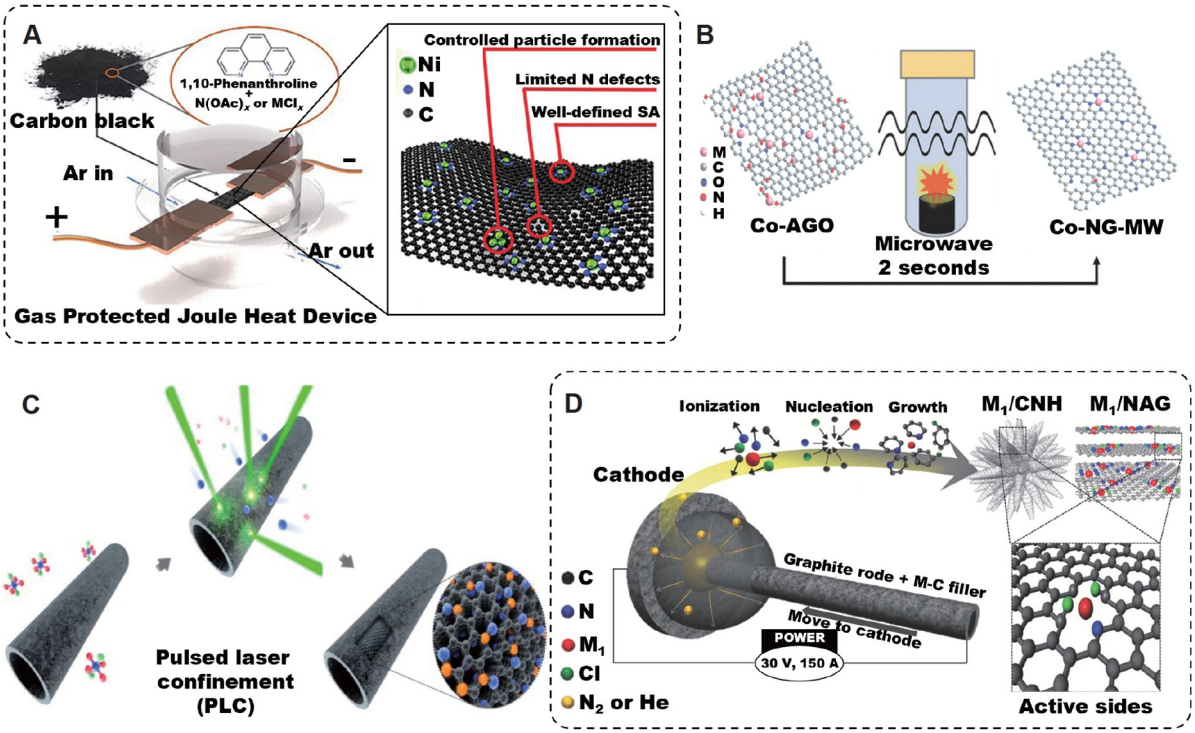

Figure 7 Representative ultrafast synthesis strategies for preparing NPM-SACs/CS. (A) Synthesis of Ni-N-C moieties supported on carbon black by current heating. Reproduced with permission from ref. [112]. Copyright©2022, John Wiley and Sons. (B) Synthesis of Co-NG-MW by two-second microwave heating. Reproduced with permission from ref. [113]. Copyright©2018, John Wiley and Sons. (C) Synthesis of Co-P SACs by PLC operation. Reproduced with permission from ref. [114]. Copyright©2019, American Chemical Society. (D) Synthesis of Fe, Co, Ni, and Pt SACs by arc discharge. Reproduced with permission from ref. [115]. Copyright©2021, John Wiley and Sons.

Characterization techniques for NPM-SACs/CS

To observe the dispersion, valence state distribution, and coordination states of metal atoms in NPM-SACs/CS, some advanced characterization techniques, such as scanning tunneling microscopy (STM) and aberration-corrected high-angle annular dark-field scanning transmission (AC HAADF-STEM), are required. Among them, electron microscopy is used for morphological observation, X-ray absorption spectroscopy (XAS) is used for atomic structure and electronic property studies, and other specific characterizations for auxiliary analysis.

STM

STM is a microscopic device with ultra-high resolution at the atomic level, where the unique scanning probe structure contacts the sample and generates a tunnel currently under the condition of the applied voltage, to observe the arrangement of individual atoms on the material surface and the behavior of surface electrons in real-time. Compared with other surface analysis techniques, STM has a resolution of up to 0.1 Å in the direction parallel to the sample surface, which means that single atoms can be accurately resolved. Notably, STM can be used to observe the local surface structure of a single atomic layer, rather than the average properties of the bulk phase or the whole surface, so the surface defects and surface reconstruction can be

directly observed. For example, with 2D electrochemical STM (EC-STM), the coordination structures of single atom Fe supported on graphene were well revealed, i.e., single Fe atom trapped in two (Fe-2V), three (Fe-3V), or four (Fe-4V) neighboring carbon vacancies, and three Fe atoms trapped into a cluster of six carbon vacancies (3Fe-6V) (Figure 8A), resulting in an excellent HER catalytic activity [116]. Moreover, the 3D image of the sample surface in real space can be obtained in real-time, which can be used for the study of the surface structure with or without periodicity and the dynamic processes of surface diffusion or growth law. In another research, the underlying growth mechanism in Klein (K) and Zigzag (Z) edges of graphene sheets catalyzed by single Ni atoms was also directly uncovered by *in situ* high-speed STM (Figure 8B) [117]. Although STM has such great advantages in single-atom characterization, it is difficult to popularize because of its long sample testing cycle and expensive testing costs.

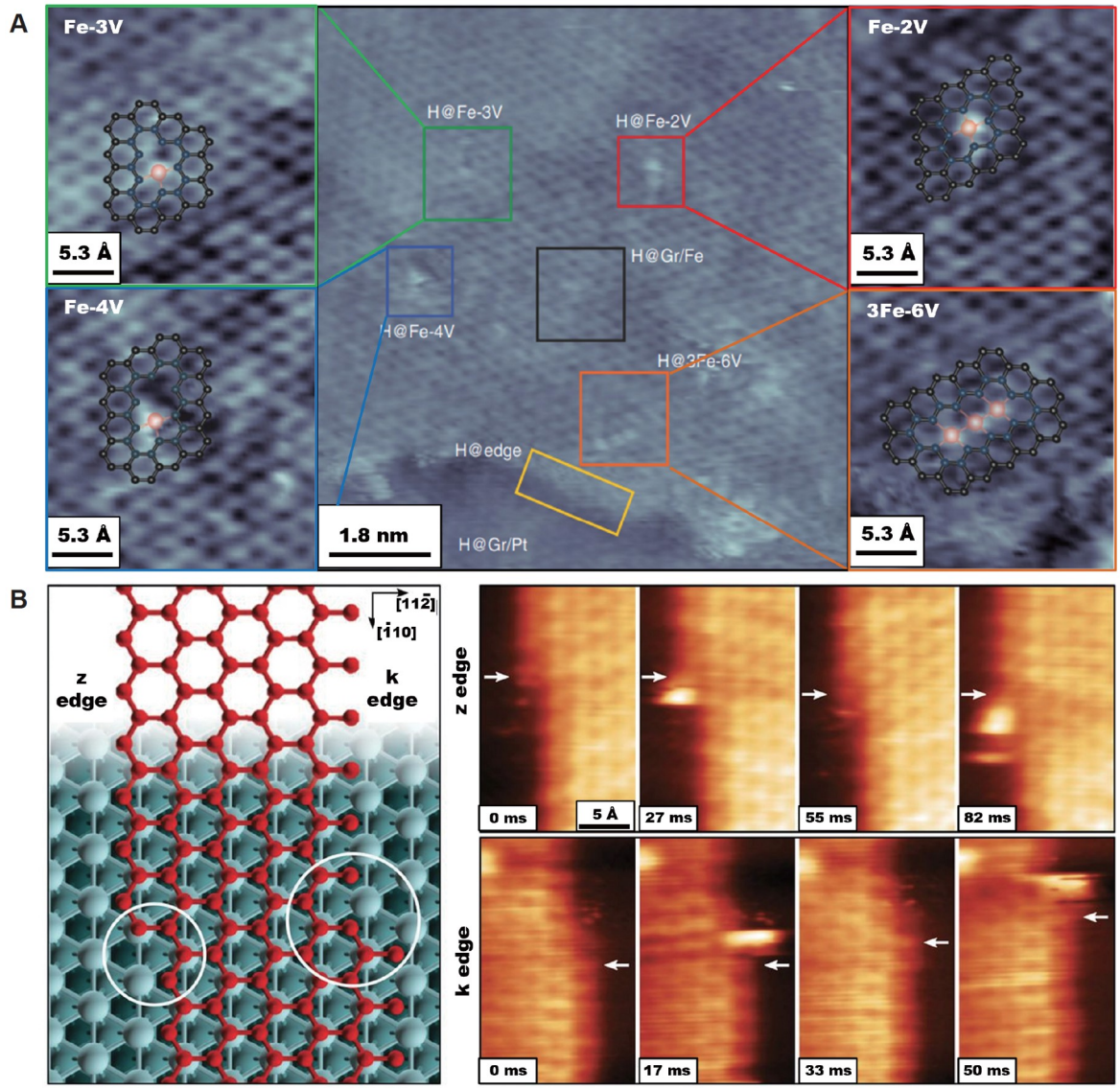

Figure 8 (A) EC-STM images of Fe SACs on graphene with four different coordination environments. Reproduced with permission from ref. [116]. Copyright©2021, Springer Nature. (B) STM images of graphene growth along Z and K edges on Ni (111) crystal face. Reproduced with permission from ref. [117]. Copyright©2018, American Association for the Advancement of Science.

AC HAADF-STEM

In addition to tunnel effect imaging, high-energy electron beam scanning and projection imaging can also be employed to observe the apparent morphology of obtained materials. The resolution of the traditional scanning electron microscope (SEM) and transmission electron microscope (TEM) cannot meet the sub-nanometer level imaging. Hence, much more attention is paid to AC HAADF-STEM with higher technical requirements and larger magnification. With the ongoing update of equipment, the resolution of AC HAADF-STEM has reached the sub-angstrom (0.5 Å) level, allowing it to recognize the isolated metal atom on the surface of carbon material. AC HAADF-STEM is usually used in combination with energy-dispersive X-ray spectrometry (EDX) and electron energy loss spectroscopy (EELS) to reveal the composition and distribution of elements visually. Chen *et al*. [118] observed that small bright spots (Fe-N_4 sites) were uniformly dispersed with nearby big bright spots (Fe_3C nanoplates) in the carbon matrix using HAADF-STEM and elemental mapping (Figure 9A). Furthermore, Wang *et al*. [119] investigated the composition of bright spots and nearby dark shadows in AC HAADF-STEM image through EELS analysis, in which the coexistence of Co, N, and C in bright spots and the only C component in dark shadow revealed the formation of CoN_x moiety on carbon matrix (Figure 9B).

XAS

In view of the different absorption characteristics of each element to X-ray, the elemental composition, electronic state, and microstructure of materials can be accurately analyzed by virtue of recording the changes of the signal before and after the X-ray incident. In recent years, XAS based on synchrotron radiation equips with some merits of low signal-to-noise ratio, high resolution, and rapid detection, which shows great advantages in confirming the local atomic structure and the chemical state of SACs. According to the research needs, XAS can be divided into two types: extended X-ray absorption fine structure (EXAES) with the high-energy side of the element absorption edge ranging from 30 to 1000 eV and X-ray absorption near-edge structure (XANES) within 50 eV of the absorption edge [120]. Both EXAES and XANES can reflect the coordination environment of SACS, but they have different divisions of labor. EXAFS is mainly used to calculate key parameters such as coordination number and bond length between isolated metal atoms and carbon matrix, while XANES is used to obtain valence and geometric information of isolated metal atoms [71,77,82,95]. Up to now, a series of metal-N_x ($CoN_{2,3,4}$, CoN_5, FeN_4, FeN_5) [121–123], MN_xO_y (CuN_2O_2, NiN_2O_2, and FeN_4O) [70,72,124], metal-N_xS_y (FeN_3S, CoN_4S) [72,91,99] and metal-O_xS_y (CuO_3S) [93] moieties have been precisely identified by those two means. For example, the bonding structure of N, O-coordinated Cu SACs (i.e., Cu-CDs) synthesized by partially carbonizing $Na_2[Cu(EDTA)]•2H_2O$ was confirmed by EXAFS spectra and backscattering paths fitting analysis [70]. As shown in Figure 10A, the existence of a Cu-N/O peak and the absence of a Cu-Cu peak in the Fourier-transform EXAFS (FT-EXAFS) spectrum revealed that the bonding structure of Cu-CDs was CuN_xO_y. Since Cu-O and Cu-N have similar bond lengths, wavelet transform EXAFS (WT-EXAFS) failed to further analyze their fine structure though resolving the backscattered atoms (Figure 10B). Finally, three structures of CuN_1O_3, CuN_2O_2, and CuN_3O_1 were constructed to seek out the best matching structure (CuN_2O_2) by FT-EXAFS backscattering fitting (Figure 10C). For XANES studies, Li group [121] found that the XANES curve of Co-N_5 was between that of

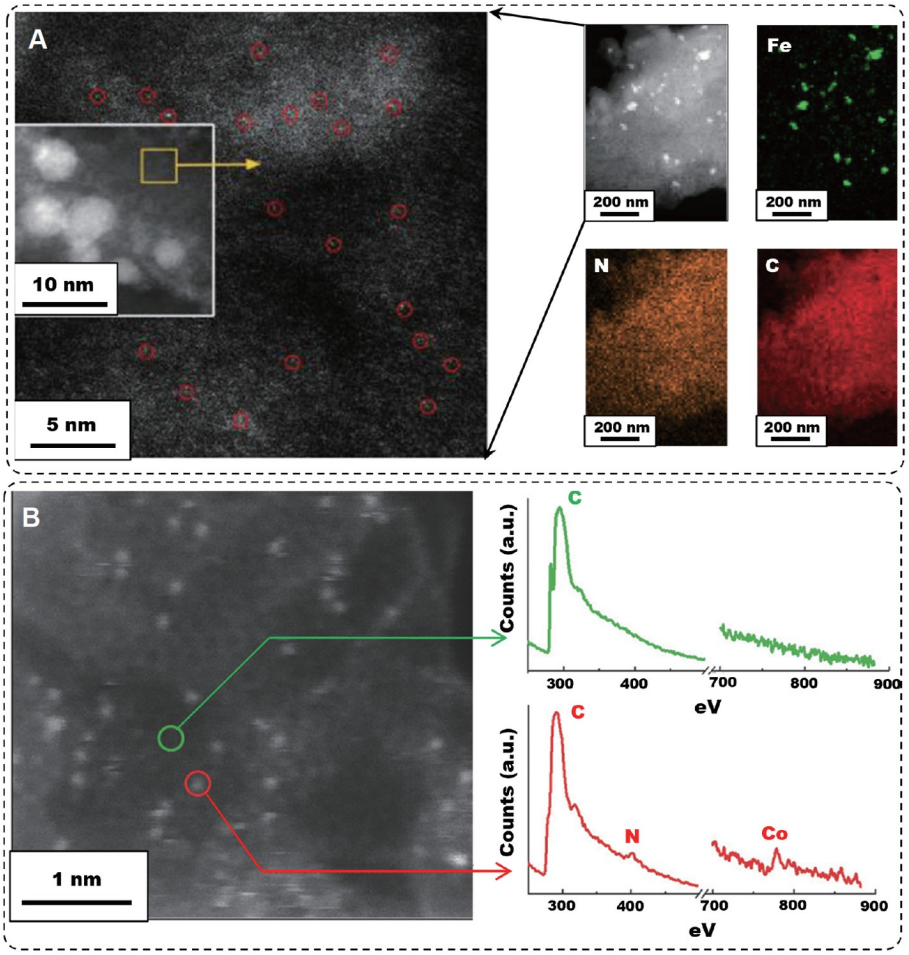

Figure 9 (A) AC HAADF-STEM image (inset: TEM image) and corresponding element mapping of FeN_4-Fe_3C catalyst. Reproduced with permission from ref. [118]. Copyright©2022, John Wiley and Sons. (B) AC HAADF-STEM image and corresponding EELS point spectra of Co SAC. Reproduced with permission from ref. [119]. Copyright©2018, John Wiley and Sons.

CoO and Co_3O_4, inferring the chemical valence of isolated Co atom in the Co-N_5 sites was between +2 and +3 (Figure 10D). By comparing the XANES spectra of Fe-N_4 and FePc precursor at 7118 eV, Zhao *et al.* [122] concluded that FePc with a strong square plane structure distorted the D_4h symmetry with the axial ligand after pyrolysis (Figure 10E).

X-ray photoelectron spectroscopy

In addition to XANES, X-ray photoelectron spectroscopy (XPS) can also be served to detect the valence of elements in local regions. XPS, by contrast, records the information of free photoelectrons which escape from atomic layers on the surface of material induced by an X-ray incident. Therefore, XPS can provide certain help for understanding the valence state and charge distribution information of isolated metal atoms mono-dispersed on the surface of carbon material. Wang *et al*. [72] verified the conclusions of XAS with the aid of XPS analysis. The XPS fine spectrum of N 1s was well-deconvoluted into four separate peaks, i.e., pyridinic nitrogen, Ni-N, pyrrolic nitrogen, and graphitic nitrogen located at 398.2, 399.5, 400.5, and 401.1 eV,

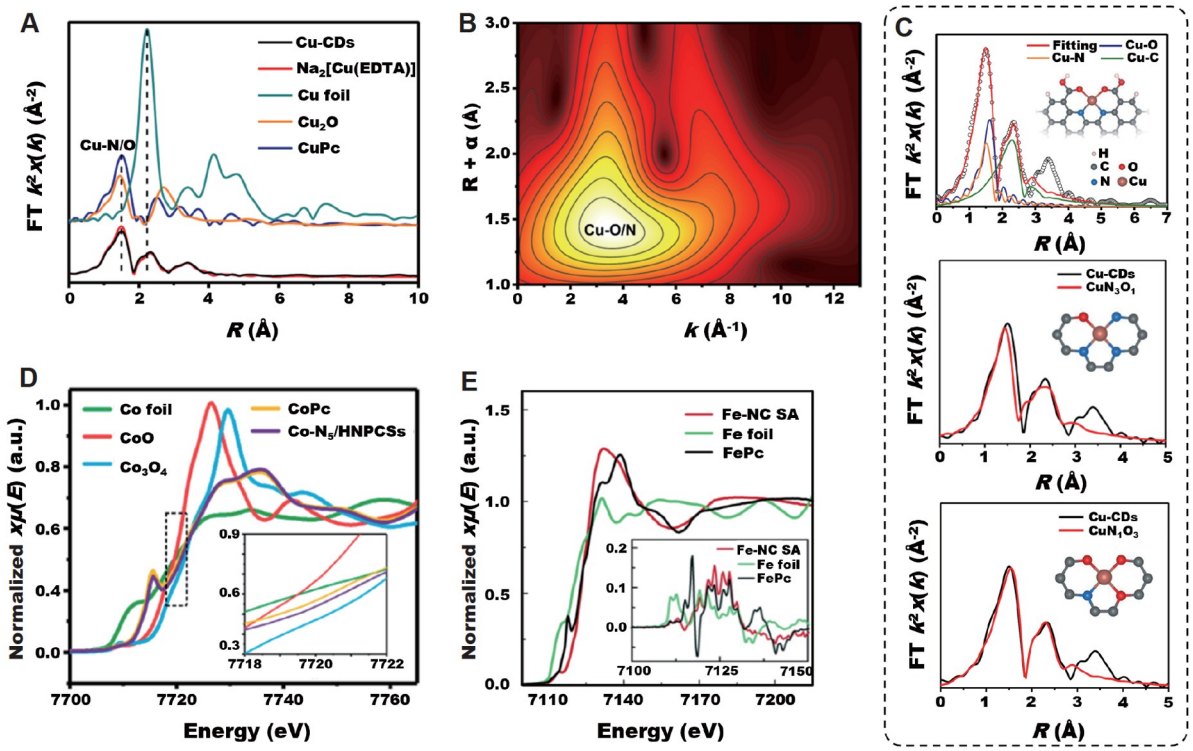

Figure 10 (A) FT-EXAFS image of Cu-CDs and control samples at Cu K-edge, (B) WT-EXAFS image of Cu-CDs, and (C) FT-EXAFS backscattering fitting images of three constructed structures: CuN_2O_2, CuN_3O_1, and CuN_1O_3. Reproduced with permission from ref. [70]. Copyright©2021, Springer Nature. (D) XANES image of Co-N_5/HNPCSs and control samples at Co K-edge. Reproduced with permission from ref. [121]. Copyright©2018, American Chemical Society. (E) XANES image of Fe-NC SAC, Fe foil, and FePc at Fe K-edge. Reproduced with permission from ref. [122]. Copyright©2019, Springer Nature.

respectively (Figure 11A), of which the fitting method is common in other researches [125,126]. In addition, the relatively high level of pyrrolic nitrogen peak revealed that Ni atoms are mainly coordinated with pyrrolic nitrogen to form the NiN_2O_2 structure. Most interestingly, the peaks of Ni $2p_{1/2}$ orbital and Ni $2p_{3/2}$ orbital in the Ni 2p spectrum can be perfectly fitted to Ni^{2+}, indicating that the isolated Ni atoms existed in the form of Ni^{2+} in the NiN_2O_2 structure, which was in line with the results of XANES.

In addition to visually reflecting changes in valence, XPS can also provide other reference information. With the help of XPS technology, Dong and coworkers [127] calculated that the atomic percentage of Fe and N elements dispersed on the surface of cubic carbon frameworks was 0.8% and 3.9%, respectively. Yin and coworkers [109] found an apparent shift of pyrrolic nitrogen, Co $2p_{1/2}$ and Co $2p_{3/2}$ peak in Co-NPs/N-C with respect to that in Co-SAs/N-C (Figure 11B), which may provide an extra approach to distinguish metal single atoms from their nanoplates counterparts.

Mössbauer spectroscopy

Mössbauer spectroscopy records the information of nuclear gamma rays with almost recoil-free emission and absorption in solid materials. Considering the super sensitivity of Mössbauer spectroscopy to the coordination environment and electronic configuration of central iron ions in complex materials, it exclusively

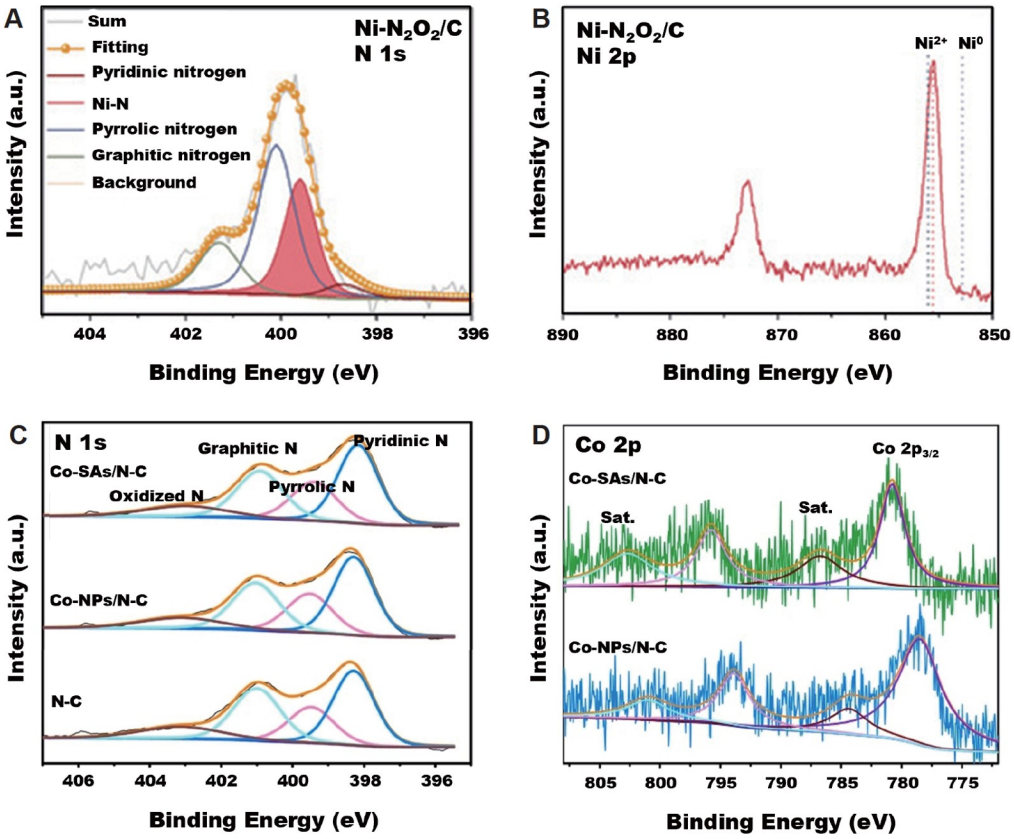

Figure 11 (A) N 1s and Ni 2p XPS fine spectra of Ni-N_2O_2/C. Reproduced with permission from ref. [72]. Copyright©2020, John Wiley and Sons. (B) N 1s and Co 2p XPS fine spectra of Co-SACs/N-C and control samples. Reproduced with permission from ref. [109]. Copyright©2020, Springer Nature.

provides strong support for the characterization and analysis of Fe-based SACs. For instance, Yu and colleagues [128] found that the Mössbauer spectroscopy of Fe-PPy SACs can be well-fitted to two sets of peaks (Figure 12A), corresponding to the coordination configuration of Fe-N_4. While the Mössbauer spectroscopy of Fe SACs obtained by carbonizing iron porphyrin complexes was deconvoluted into three doubtless (D1, D2, D3) and one single (D4) [129]. Among which, D1 was indexed to FeN_4 sites with ferrous low-spin, the two ferrous mid-spin FeN_4 sites of D2 and D3 were equipped with analogous iron phthalocyanine and iron porphyrins coordination environment, the little D4 was ascribed to the impurity of magnetic iron on the material surface. Notably, Mössbauer spectroscopy demonstrated that these iron impurities were successfully removed by further calcination under N_2 and H_2 atmospheres (Figure 12B).

In situ characterization

As mentioned above, due to the high dispersion, low loading, and sub-nanometer size of monatomic materials, ordinary characterization methods such as IR, XRD, TEM, and Raman cannot meet the requirements of detection, and the results are often unsatisfactory. Recent studies have shown that compared with *ex situ* characterization, *in situ* characterization has an unexpected effect on SACs by detecting the sample dy-

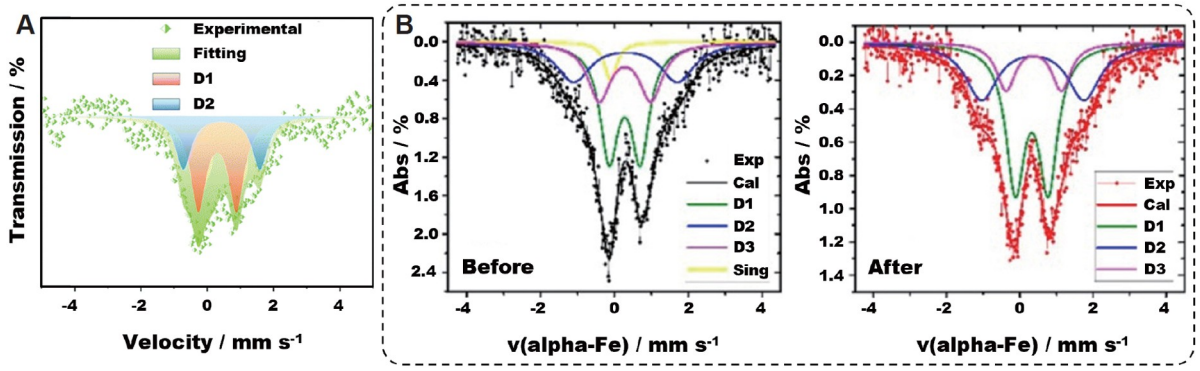

Figure 12 (A) Mössbauer spectroscopy image of Fe-PPy SAC. Reproduced with permission from ref. [128]. Copyright©2021, Royal Society Chemistry. (B) Mössbauer spectroscopy images of alpha-Fe SAC before and after N_2 and H_2 atmospheres calcination. Reproduced with permission from ref. [129]. Copyright©2016, American Chemical Society.

namics. At present, these *in situ* representations mainly focused on the study of noble metal-based SACs, such as the discrimination of single atoms and clusters as well as the conversion of the former to the latter by *in situ* Fourier-transform infrared spectroscopy (FTIR) [29,130], detection on physicochemical properties of single atoms before and after catalysis by *in situ* X-ray diffraction (XRD) and *in situ* Raman [131,132], the study of the growth rule of single atoms on support by *in situ* TEM [133]. It is believed that in the future, these techniques will be applied to the study of non-precious metals SACs.

Combined with *in situ* FTIR characterization, the three characteristic peaks formed by the interaction between CO and Pt SACs at 2030, 1860, and 1950 cm^{-1} were attributed to the linear bound CO at the single Pt site, the bridge CO on the two Pt atoms and the CO adsorbed at the interface between Pt cluster and carrier, respectively [29]. The presence of bridging CO and the blue shift phenomenon of linear bound CO frequency with decreasing CO pressure indicated the convention of single Pt atom to Pt clusters in the catalyst. It is believed that in the future, these techniques will be applied to the study of non-precious metals SACs (Figure 13A). Combined with *in situ* XRD analysis, in a long process of Pt/MoC catalyzing CO and H_2O to prepare H_2, the color signal of each diffraction peak of the catalyst is uniform and consistent, indicating the stable catalytic ability of Pt SACs (Figure 13B) [131]. Combined with *in situ* Raman spectrum, the stabilization effect of N-heterocyclic carbene molecules (NHCs) ligand on Cu SACs at different CO_2RR potentials was determined [132]. The characteristic Cu-OH peak located at 409.2 cm^{-1} kept almost the same under different reduction potentials, indicating the excellent stability of Cu coordination structure (Figure 13C). Combined with *in situ* TEM technique, the evolution of Pt clusters converted to Pt single atoms with facile reduction of the H_2/N_2 mixture at 200°C on Ru nanoparticle branches was well monitored [133]. The Pt clusters showed a tendency of collapse in the third second after the reduction reaction, with obvious collapse at 11.2 s, complete collapse at 22.3 s, and complete mono-dispersion on the Ru crystal plane at 37.2 s (Figure 13D). Although these advanced techniques have only been reported in the characterization of noble metal SACs, it is believed that with in-depth research, they will be widely used in the study of NPM-SACs/CS in the near future.

Density functional theory calculation

Density functional theory (DFT) calculation is an auxiliary tool to reveal the catalytic activity and the reaction mechanism. DFT can not only reveal the spin configuration and geometric interactions between

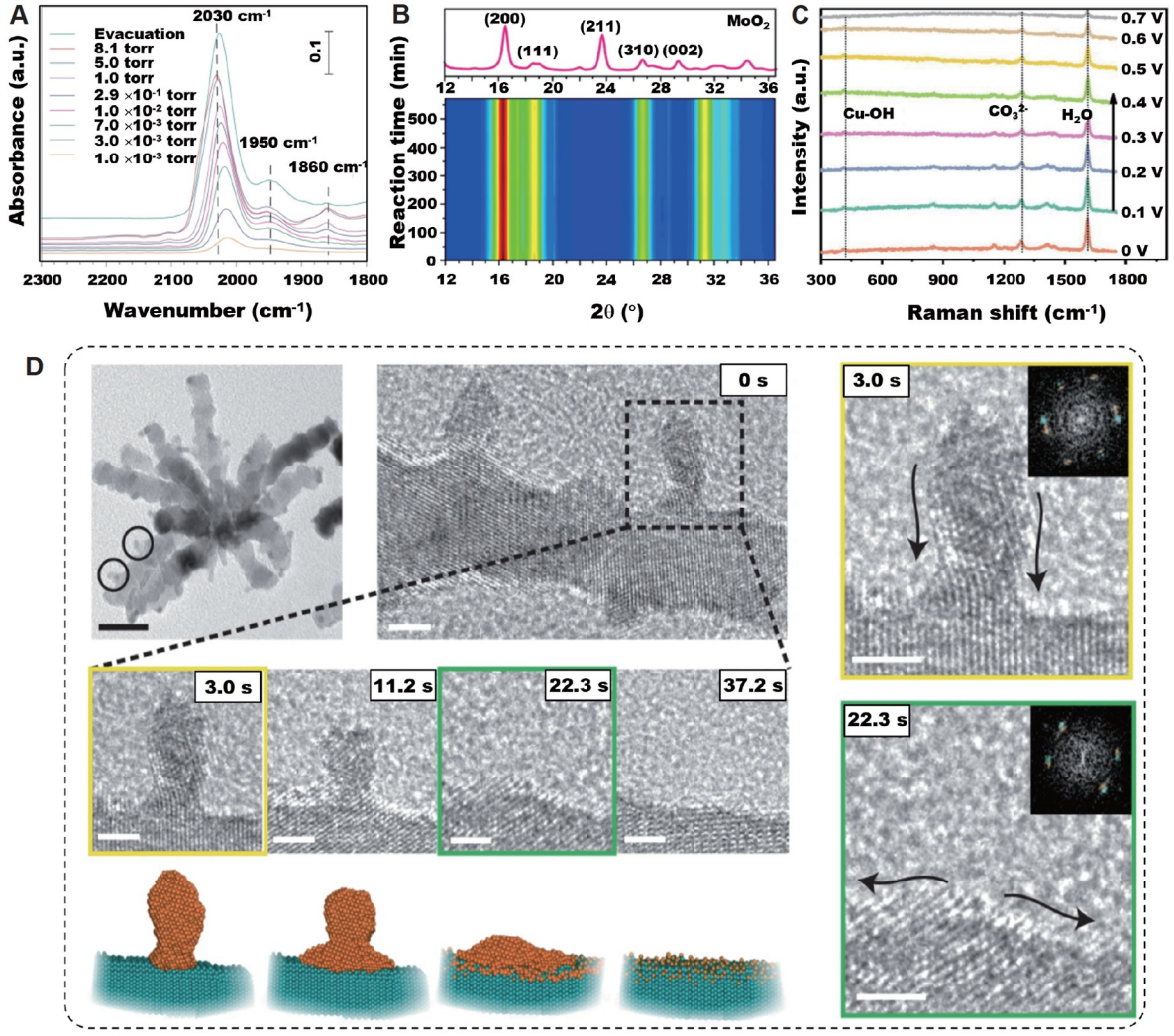

Figure 13 Representative *in situ* characterization methods of SACs. (A) *In situ* FTIR characterization of Pt SACs [29]. Copyright©2011, Springer Nature. (B) *In situ* XRD characterization of Pt/MoC. Reproduced with permission from ref. [131]. Copyright©2021, Springer Nature. (C) *In situ* Raman characterization of Cu SACs. Reproduced with permission from ref. [132]. Copyright©2021, John Wiley and Sons. (D) *In situ* TEM characterization of single Pt atoms on Ru nanoparticles. Reproduced with permission from ref. [133]. Copyright©2022, Springer Nature.

monodisperse metal sites and carbon supports, but also reveal the mechanism of reactant adsorption and product desorption on the active site. On the basis of these features, it is possible to design NPM-SACs/CS with strong activity, high selectivity, and desirable stability with DFT calculation.

Revelation of catalytic activity and reaction mechanism

The electronic properties and geometric configuration are important factors affecting the catalytic activity of SACs. It is a common method to analyze the charge/spin density, energy band and density of states (DOS) qualitatively and quantitatively through DFT calculation to further explore the attribution of its properties. The spin state can be used to describe the spin potential configuration of d orbital electrons in metal atoms,

which is a basic electron characteristic of SACs. Different spin states usually have different energies and different reaction barriers, leading to different catalytic effects. Gong *et al*. [134] found that the spin state of high-valence Co was more conducive to the adsorption of $HCOOH_{ads}$ intermediates and reduced CO_2 to HCOOH with high selectivity (Figure 14A). Li *et al*. [135] highlighted that the spin moment of Fe SACs plays an important role in N_2 adsorption and subsequent activation, and the low-coordination FeN_3 showed better NRR activity due to the rather greater and more centralized spin moment. Recently, Han *et al*. [136] proposed that cooperative spin transitions between the neighboring Fe atoms can influence the spin configuration and thus the ORR activity of each Fe sites because of the larger magnetic exchange interaction. Compared with the complex spin state analysis, DOS can clearly and intuitively indicate the intrinsic activity

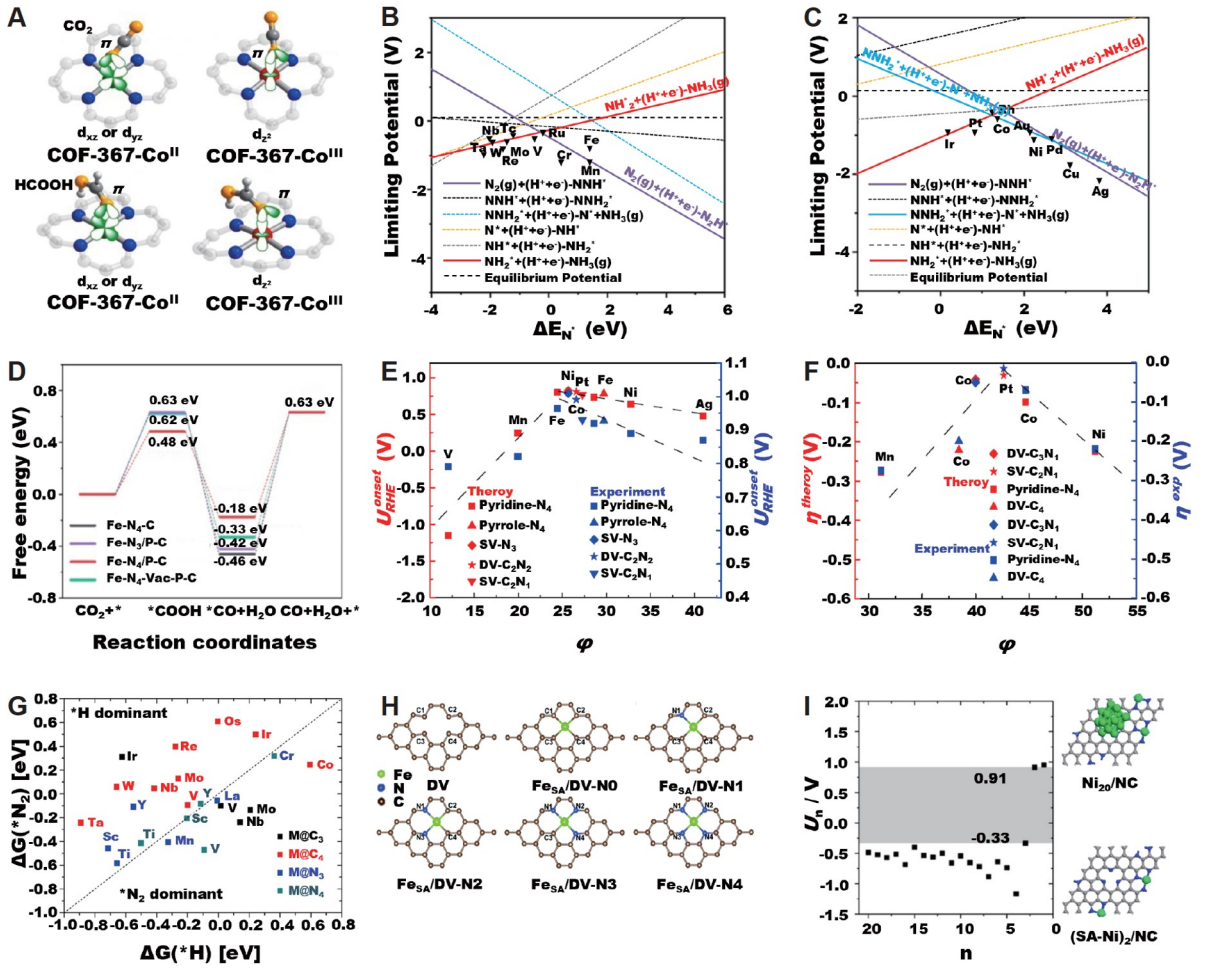

Figure 14 Coupling modes of (A) CO_2 and HCOOH absorbed on COF-367-Co^{II} and COF-367-Co^{III}. Reproduced with permission from ref. [134]. Copyright©2020, American Chemical Society. Limiting potentials of (B) early transition metal and (C) late transition metal. Reproduced with permission from ref. [139]. Copyright©2019, American Chemical Society. (D) Absorption volcano graph of Fe-N_4-C, Fe-N_3/P-C, Fe-N_4/P-C, and Fe-N_4-Vac-P-C for the electroreduction of CO_2 to CO. Reproduced with permission from ref. [140]. Copyright©2022, American Chemical Society. Theoretical and corresponding experimental (E) onset potentials for ORR and (F) overpotentials for HER vs. the descriptor φ. Reproduced with permission from ref. [141]. Copyright©2018, Springer Nature. (G) Calculated ΔG(*H) and ΔG(*N_2) on SACs. SACs in *N_2 dominant region (under the dashed line, ΔG(*H) > ΔG(*N_2)) correspond to N_2 adsorption being more favorable than *H formation at 0 V (vs. RHE). Reproduced with permission from ref. [142]. Copyright©2018, American Chemical Society. (H) Bare carbon substrate and five different Fe-N-C coordination structures. Reproduced with permission from ref. [143]. Copyright©2020, Royal Society of Chemistry. (I) Electrochemical potential window of Ni/NC and the corresponding model of Ni_{20}/NC and (SA-Ni)$_2$/NC). Reproduced with permission from ref. [144]. Copyright©2020, American Chemical Society.

of metal sites. In general, DOS near the Fermi level helps to identify specific atoms that contribute to the state, which significantly improve the catalytic dynamics [137]. Zhang *et al.* [138] concluded that the DOS of the monodisperse Ni atoms on the graphene surface was much higher than that of Ni(111) near Fermi energy. This highly dispersed Ni-N-C coordination structure effectively inhibits other competitive reactions and significantly improves the selectivity of CO_2 to CO.

In addition to the analysis and evaluation of catalyst activity, DFT calculations are also essential in the process of speculating the catalytic mechanism. The energy parameter distributions of SACs in a certain reaction were served by theoretical calculation to infer the specific catalytic path, and Gibbs free energy, enthalpy change and zero point energy are commonly used energy parameters, which can be obtained by structural optimization and frequency calculation for all preset reactants, products, intermediates and transition states along the reaction path. The determination of the rate-limiting step is the key to predict the reaction path. Liu *et al*. [139] reported a comprehensive profile of 20 types NPM-SACs on three different carbon substrates for electrocatalytic NRR, and calculated the negative of the free energy change of each proton-coupled electron transfer step, i.e., limiting potential. The impact of different metal centers on the limiting potential was systematically summarized. In a relatively negative range (−4–0 eV) of ΔE_{N*}, most SACs underwent a potential-limiting step of $*NH_2 + H^+ + e^- \rightarrow NH_3$ (g), while in 1–4 eV, Co, Ag and Ni SACs underwent a potential-limiting step of $*NH_2 + H^+ + e^- \rightarrow NH_3$ (g), and Cu, Ag SACs underwent a potential-limiting step of N_2(g) + ($H^+ + e^-$) → *NNH step (Figures 14B and 14C). To understand the mechanism of Fe-N/P-C structure reducing the activation energy of CO_2RR, Li *et al*. [140] calculated the adsorption energy of Fe SACs with different P-regulated coordination structures on *COOH and *CO intermediates, and found that the protonation of CO_2 into *COOH was a rate-limiting step in the whole catalytic process (Figure 14D).

Design of catalysts

Strong activity, high selectivity, and desirable stability are the final objectives to design NPM-SACs/CS. Owing to the introduction of DFT, we can quickly screen and separate materials that meet the synthetic requirements, which greatly reduces the experimental workload, and in turn, the experimental data can also prove the correctness of DFT. The onset potentials of ORR and overpotential of HER from different metal single atoms with different N-coordination structures were calculated by DFT and verified by experiments. Among them, Ni SACs with pyridine-N_4 structure shows great potential for ORR, while Co SACs with DV-C_3N_1 structure stand out for ORR (Figures 14E and 14F) [141]. Based on DFT calculation, we can autonomously inhibit the competing reactions in the system according to the difference of the free energy of the catalyst for each reaction, and improve the selectivity of the reaction. For example, in the defective graphene-based SACs, Mo@C_3, Nb@C_3, V@C_3, Mn@N_3, etc., show high selectivity for NRR, resulting from their strong $*N_2$ adsorption energy and weak *H adsorption energy, which inhibited the adsorption of H at the active site, thus reducing the competition of HER in NRR (Figure 14G) [142]. With the help of DFT, the thermodynamic and kinetic parameters were calculated to determine whether dispersed single atoms agglomeration or leach and thus to evaluate the stability of the catalyst. Generally, a high energy barrier of single atoms self-aggregating or diffusing away from another site suggests that the SACs are stable against aggregation or leach. The calculated kinetic parameters reveal that the stability of Fe SACs is significantly

improved by doping N atoms into carbon-based substrates, arising from the enhanced energy barrier of iron atom migration (Figure 14H) [143]. In addition, the leaching stability of metal atoms or clusters can be defined according to the electrochemical potential window boundary between the highest leaching equilibrium potential corresponding to the formation of atom-dispersed structure and the lowest equilibrium potential corresponding to the destruction structure, of which the rule is broadly applicable to a variety of metals on different substrates (Figure 14I) [144].

The vigorous development of DFT calculation has promoted the development of SACs, and the significance of DFT calculation in electrocatalysis is far more than the study of the interaction between the active site and adsorption intermediates and the prediction of reaction mechanism, the constantly updated algorithms and techniques are more important. Unfortunately, limited by the accuracy and efficiency of the algorithm and model construction, traditional DFT methods cannot perfectly deal with realistic catalytic surfaces and complicated reaction environments. Hence, DFT calculation can only be used for qualitative or semi-quantitative interpretation of specific electrocatalytic systems. There is still an urgent need for new computational techniques or strategies to meet the higher accuracy of the experimental measurements. At present, some new calculation methods gradually took many external factors into consideration, such as temperature, pressure, solvation effect and electrode potential [145–147], and put forward a novel pseudo-adsorption and long-range redox coupling mechanisms [148], which greatly enrich the methodology and application of DFT. Moreover, the combination of DFT calculation and machine learning is a new trend to achieve efficient and accurate computing, where machine learning will provide a new platform for designing NPM-SACs/CS accurately and efficiently [149,150].

Structure adjustment strategy of NPM-SACs/CS

To optimize the catalytic performance, the electron structure of NPM-SACs/CS (defined as the micro-environment), as well as the morphology and structure of the carbon matrix (defined as the macro-environment), have been extensively and deeply studied [151,152]. This section summarizes strategies to optimize the macro- and micro-environment of NPM-SACs/CS. The microenvironment here mainly includes adjusting the type of central metal atom, changing the coordination number of a nitrogen atom, building non-nitrogen heteroatom coordination, adjusting carbon basal plane, and building bimetallic sites.

Tuning the types of central metal atoms

Currently, various non-precious metal atoms, like Fe, Co, Ni, Cu, Zn, etc., have been explored as the central metal atoms of NPM-SACs/CS. The central metal atom of NPM-SACs/CS plays a huge part in the electrocatalytic performance. The different metal species have different electron configurations, which would influence electrocatalytic activity and selectivity [63]. Therefore, a suitable central metal should be selected to optimize the catalytic performance of the NPM-SACs/CS. For example, Hu and cooperators [153] prepared a series of transition metals (Fe, Co, Ni) on nitrogen-doped porous carbon (M-N-C) via silica-templated pyrolysis methods. They compared the CO_2RR performance of various M-N-C SACs with different metal atoms, and reported a CO selectivity order given as Ni > Fe ≫Co. Notably, the Ni-N-C

performed a high CO selectivity with a Faradaic efficiency of 93%.

Changing the coordination numbers of nitrogen atoms

In NPM-SACs/CS systems, central metal atoms and nearby light atoms interact via direct d-p orbital hybridization in the first coordination sphere. The tuning strategy of the first coordination shell provides straight electronic and steric effects to modulate the adsorption/desorption capabilities of intermediates at the metal sites [154]. By exploring vast NPM-SACs/CS systems, the most typical coordination type between the central metal atoms and carbon substrate was a four-coordinated symmetric plane M-N_4 configuration, similar to naturally occurring porphyrins and enzymes [155]. Meanwhile, the catalytic performance of NPM-SACs/CS could be further tuned by changing the number of coordination nitrogen atoms. For example, Co-SACs with Co-N coordination numbers ranging from 4 to 2 were designed by adjusting the pyrolysis temperature [156]. Results showed that CoN_2 sites far outperformed those of CoN_3 and CoN_4 toward CO_2RR because the lower coordination number was favorable for the activation of CO_2 to the CO^{2-} intermediate and thereby improving the catalytic performance.

Constructing heteroatoms coordination

The coordination of N atoms could be partially substituted by other heteroatoms (O, S, P, B, etc.) in the first shell of SACs, which could further break the symmetry and tune the electron density to optimize the catalytic activity [154]. The dual coordination atoms can make the asymmetric four-coordinating configuration structure with improved catalytic performance, maybe because of the different electron spin density and electronegativity of the dual coordination atoms. For instance, Yuan and co-workers [157] prepared N and P dual-coordinated iron active sites (Fe-N/P-C) on carbon nanosheets and determined them by X-ray absorption fine structure analysis. DFT calculations illustrated that the O_2 molecules can be easily adsorbed and strongly bonded on Fe-N_3P active sites, due to the free energies of O_2 molecules caught by Fe-N_4 and Fe-N_3P being −1.19 and −1.01 eV, respectively. Furthermore, *OH detached into OH^- was the rate-determining step of the ORR, where the free energy of Fe-N_3P active sites was 0.85 eV, much lower than that for Fe-N_4 (1.02 eV), indicating that the ORR catalytic activity of Fe-N_3P was higher than that of Fe-N_4. As a result, the new catalysts with rich FeN_3P active sites exhibited an excellent ORR performance with an onset potential of 0.941 V and a half-wave potential of 0.867 V in 0.1 mol L^{-1} KOH, which is superior to those of the commercial Pt/C benchmark.

Adjusting the carbon basal plane

Besides the direct coordination with metal atoms, indirectly coordinated heteroatoms in the carbon basal plane can also affect the electronic structure of the metal sites through long-range delocalization [54]. In addition, intrinsic carbon vacancy near the metal center can bring about the electron redistribution of the metal atoms, thereby altering the interaction between the active site and the intermediate [158]. Therefore, vacancy defective carbon materials can provide optimized support for the construction of highly active SACs by creating surrounding defects. To form the defect sites, well-defined carbon structures like graphene or

CNTs could reduce their size or fabricate hole defects by balling, chemical or plasma etching means. For instance, Pan *et al*. [159] reported an H_2O_2 etching strategy for the construction of Fe-N_4 SACs on graphene oxide with defective nanopores, which exhibited high activity for CO_2RR to CO (94% FE at −0.58 V). Compared with the Fe-N_4 anchored on a well-defined graphene substrate, the Fe-N_4 anchored on the graphene with vacancies showed a downshifting of the d-band center of Fe sites, weakening the adsorption of CO intermediate over Fe sites and thereby enhancing the CO_2RR activity.

Constructing dual metal sites

Dual metal sites composed of direct bonding or indirect coupling could provide unique properties of NPM-SACs/CS, like optimizing binding energy during the catalysis process and supplying diverse active sites with distinct functionalities for the multiple-step reactions [160]. Constructing the dual metal site catalyst was largely dependent on the choice of the precursors and the synthesis condition. At present, the dual metal site of NPM-SACs/CS can be divided into three types: direct bonds between the same metal atoms, direct bonds between different metal atoms, and metal atoms separated by light atoms forming M-light atom-M atomic structure. For example, Wang *et al*. [161] represented an electrocatalyst with Fe-Co dual sites embedded on N-doped porous carbon by a host-guest strategy. The synthesis is based on control over bonding between Co nodes (host) and adsorbed Fe ions (guest) within the confined space of MOFs. The experimental and theoretical analysis confirmed the existence of atomically dispersed Fe/Co dual sites, where the coordination numbers of Fe-N, Co-N, and Fe-Co were about 3, 3, and 1. The prepared dual metal site catalyst exhibited a superior ORR performance compared with commercial Pt/C in 0.1 mol L^{-1} $HClO_4$ solution. The DFT calculations revealed that the dual sites were favored for the activation of O-O, which was crucial for the $4e^-$ ORR process.

Macro-environment tuning of NPM-SACs/CS

NPM supported on carbon-based materials with well-defined active sites and high atom utilization serves as a bridge between homogeneous and heterogeneous catalysis. The exploitation of carbon materials as attractive supports enables adequate exposure of single metal sites and accelerates mass transfer during catalysis. The dimensional manipulation of carbons would directly affect their properties, like the porous structure, specific surface areas, electrical conductivity, and mechanical/thermal properties, which were crucial to the catalytic activity and stability of these NPM-SACs/CS [2,60]. Currently, structural controlling strategies of carbon materials offer opportunities for the fabrication of different dimensional NPM-SACs/CS. Carbon materials with various dimensions, such as 0D (graphene quantum dots) [70], 1D (carbon nanotubes) [162,163], 2D (graphene nanosheets) [164], and 3D (porous carbon frameworks) [165,166], have been explored for the preparation of NPM-SACs/CS.

Applications of NPM-SACs/CS in energy conversion

Due to their excellent catalytic performance, NPM-SACs/CS have been explored in various critical energy-

conversion applications [58,59,167]. Here, we summarize advanced studies on the applications related to several essential reactions for energy conversion, including carbon dioxide reduction reaction (CO_2RR), hydrogen evolution reaction (HER), oxygen evolution reaction (OER), oxygen reduction reaction (ORR), and nitrogen reduction reaction (NRR).

CO_2RR

The continuous increase of carbon dioxide released by human activities makes the global climate fluctuate, disturbs the carbon balance, and poses a huge threat to human existence [168–170]. Consequently, exploring ways to convert CO_2 to fuels or other value-added chemicals is critical to mitigating the above problems. Electrochemical CO_2RR has been regarded as one of the most attractive strategies thanks to its multiple advantages such as ease of operation, mild operating conditions, and tunable products [171–174]. So far, the development of efficient and stable catalysts remains at the heart of current research. Over the past few decades, a broad range of nanostructured catalysts has been explored for CO_2RR, such as metals [175–177], metal oxides [178,179], chalcogenides [180,181], and carbon-based nanomaterials [70,182]. Among these catalysts, there is a unique class of catalysts that has attracted increasing attention over the past few years, namely SACs [173,183]. Here, we would discuss the typical works of NPM-SACs/CS for converting CO_2 to different products.

The two-electron reduction products include CO and formate, the two simplest fuels in CO_2RR [179,184,185]. Particularly, CO is the most common product of NPM-SACs/CS for CO_2RR. The activity of CO production mainly depends on the metal sites. Typically, the NPM-SACs/CS based on the Ni, Co, and Fe metal centers are the most explored to produce CO, showing excellent catalytical performances [186]. For example, Chen *et al*. [187] developed an atomically Ni-N_4 on the mesoporous carbon for CO_2RR, which showed a large CO partial current density of 366 mA cm^{-2} with a FE of CO > 95% in a flow cell. Besides, another two-electron product, the formate, has also received broad attention in NPM-SACs/CS because of its critical role in energy conversion. Presently, main group metals, like Bi, Sn, In, and Sb, have recently aroused great interest among researchers because of the moderate adsorption energies of HCOO* intermediates on their surfaces [188]. For instance, Zhang *et al*. [189] prepared In single-atom catalysts with $In^{\delta+}$-N_4 active sites on an N-doped carbon matrix derived from MOFs, which could reach a high formate FE of 96% at −0.65 V vs. RHE. In addition, In-SAs/NC (0.71 eV) had the lowest free energy for the HCOO* production followed by In-NPs/NC (0.91 eV) and NC (1.41 eV), which clearly explained the experimentally detected electrochemical performance trend of three catalysts, i.e., In-SAs/NC > In-NPs/NC > NC. These DFT calculations provided the very necessary information at the atomic scale for understanding the high activity of the designed catalysts. Furthermore, group metals like Sn and Sb were also synthesized by their developed methods, which also exhibit a formate FE over 80% in a broad potential window.

Beyond the common two-electron products, others can further be clarified as C_1 and C_{2+} chemicals. C_1 products mainly include methane and methanol, and C_{2+} products mainly include ethylene, ethanol, n-propanol, etc. Notably, CO is generally considered to play an important role in greater than two-electron reduction products [168,190]. In the NPM-SACs/CS field, CO is absorbed strongly in metal centers, thereby, tending to generate C_1 (methane and methanol). For example, single Zn atoms dispersed on N-doped microporous carbon were fabricated as electrocatalysts for CO_2RR, which delivered a remarkable perfor-

mance for CH_4 generation with FE of 85%, 31.8 mA cm^{-2}, and high-stability of 35 h without an obvious current drop [191]. And DFT calculation indicated that the Zn metal center prefers to bind with O rather than the C atom, leading to the enhancement in methane production and a decrease in the generation of CO. In addition to methane, methanol products were also obtained on the NPM-SACs/CS for CO_2RR. For instance, Cu single atoms with Cu-N_4 active centers decorated on through-hole carbon nanofiber (TCNFs) had been developed as electrocatalysts for CO_2RR, which can reach a FE of 44% and −93 mA cm^{-2} partial current density towards methanol as well as long-term stability of 50 h (Figure 15A). DFT revealed that the free energy barrier of reduction of COH* to CHOH* for methanol (0.86 eV) was much lower than the step of COH* to C* (1.88 eV) for CH_4 products, suggesting Cu single atoms on these catalysts are prone to generate CH_3OH than CH_4 (Figure 15B) [192].

Cu is unique in its ability to reduce CO_2 to C_{2+} products with large yields, however, NPM-SACs/CS with Cu metal centers are rarely demonstrated to produce C_{2+} fuels production due to the essential C-C dimerization pathway greatly hindered on single Cu sites [70]. So far, only a few studies of NPM-SACs/CS with Cu metal centers for CO_2RR to C_{2+} production were reported. For example, copper single atoms decorated on N-doped porous carbon as catalysts for CO_2RR to ethanol, acetate, and acetone [193]. Especially, the record FE of acetone was reached (36.7%) and a production rate of 336.1 μg h^{-1} (Figures 15C and 15D). And the DFT calculations demonstrated that the single Cu atom with four pyrrole-N atoms was the main active site, due to the decreased free energy required for CO_2 activation and C-C dimerization (Figure 15E).

So far, CO_2RR to the deeper reduction products beyond two-electron reduction products on NPM-SACs/CS is still a big puzzle. Inhibition of the desorption of CO from the central metal atoms by enhancing the interaction between the CO* key intermediate and the central metal atoms metal is a better choice for promoting the reaction pathway towards further reduced products. It should be noted, however, that too strong a binding energy may lead to metal center intoxication, resulting in CO_2RR inactivation [194]. Besides, the conversion of CO_2 into liquid C_{2+} products has broad prospects. For increasing the selectivity of C_{2+} products on NPM-SACs/CS, the development of dual-metal atom sites may open new doors.

HER

HER is the cathode half-reaction of water electrolysis, involving a relatively easy process of two-electron transfer to produce H_2 with high purity. pH has a certain influence on the reaction process, which is reflected in the supply of hydrogen sources, such as H^+ acting in an acidic medium, while H_2O serves in an alkaline medium. As indicated in Figure 16A, the first electron undergoes a Volmer reaction process to generate intermediate H_{ads}, while according to the different transfer paths for the second electron, H_2 release can be realized through two routes, i.e., the Heyrovsky route with a slow reaction process and Tafel route with rapid reaction process. In general, the reaction path of the HER process can be determined by the Tafel slope, of which a small value (< 30 mV dec^{-1}) is indexed to the Volmer-Tafel path, and a large value (> 60 mV dec^{-1}) is assigned to Volmer-Heyrovsky path [195].

Although precious Pt-based materials still occupy the top of the pyramid of HER catalyst, non-precious metal-based materials continue to catch up without hesitation. Recently, it was reported that mono-dispersed transition metals (Ni, Fe, Co) on carbon supports have excellent HER activity and stability in the universal pH span. Zang *et al.* [196] pyrolyzed the Ni-doped g-C_3N_4 to prepare Ni SA/NC, which only required an

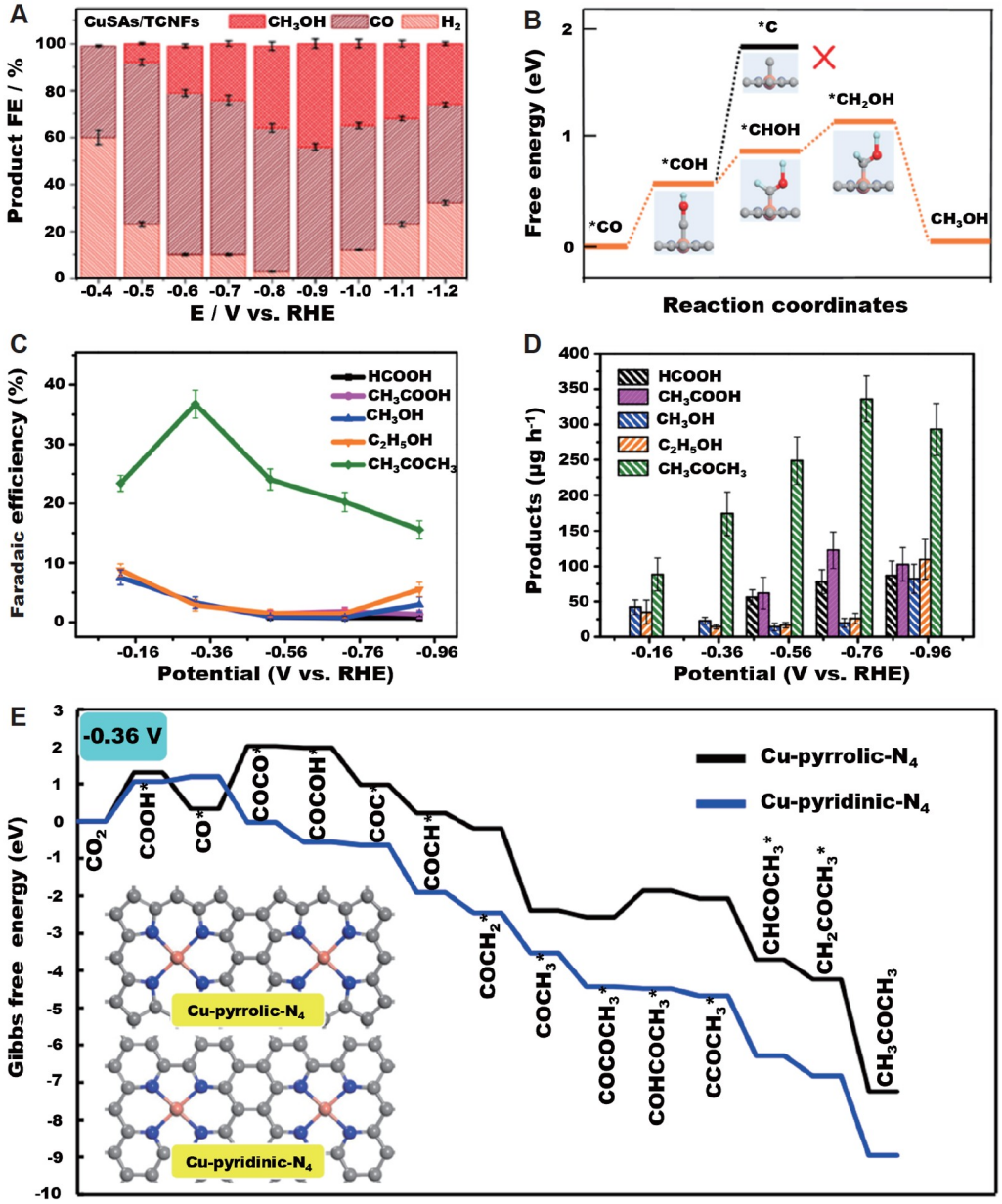

Figure 15 NPM-SACs/CS for CO_2RR. (A) Faradaic efficiencies of all products at CuSAs/TCNFs. (B) Free energies for conversion of *CO to CH_3OH on Cu−N_4 structure. Orange, gray, dark blue, red, and light blue spheres stand for Cu, C, N, O, and H atoms, respectively. Reproduced with permission from ref. [192]. Copyright©2021, American Chemical Society. Faradaic efficiency (C) and production rate (D) of CO_2 reduction products on Cu-SA/NPC. (E) Free energy diagrams calculated at a potential of −0.36 V for CO_2 reduction to CH_3COCH_3 on Cu-pyridinic-N_4 and Cu-pyrrolic-N_4 sites of Cu-SA/NPC (the computational models were included in the figure). Reproduced with permission from ref. [193]. Copyright©2021, Springer Nature.

overpotential of 105 mV to drive a current density of 10 mA cm^{-2} for HER in N_2-saturated 1 mol L^{-1} KOH (Figure 16B). Ni SA/NC exhibited an obvious superiority in large current catalysis concerning the Pt/C electrode, of which the performance output remained highly consistent after 5000 cycles of testing (Figures 16C and 16D). In addition, Ni SA/NC also has an efficient catalytic effect on hydrogen production by seawater electrolysis (Figure 16E). Xue *et al*. [197] introduced a novel HER catalyst of mono-dispersed zero

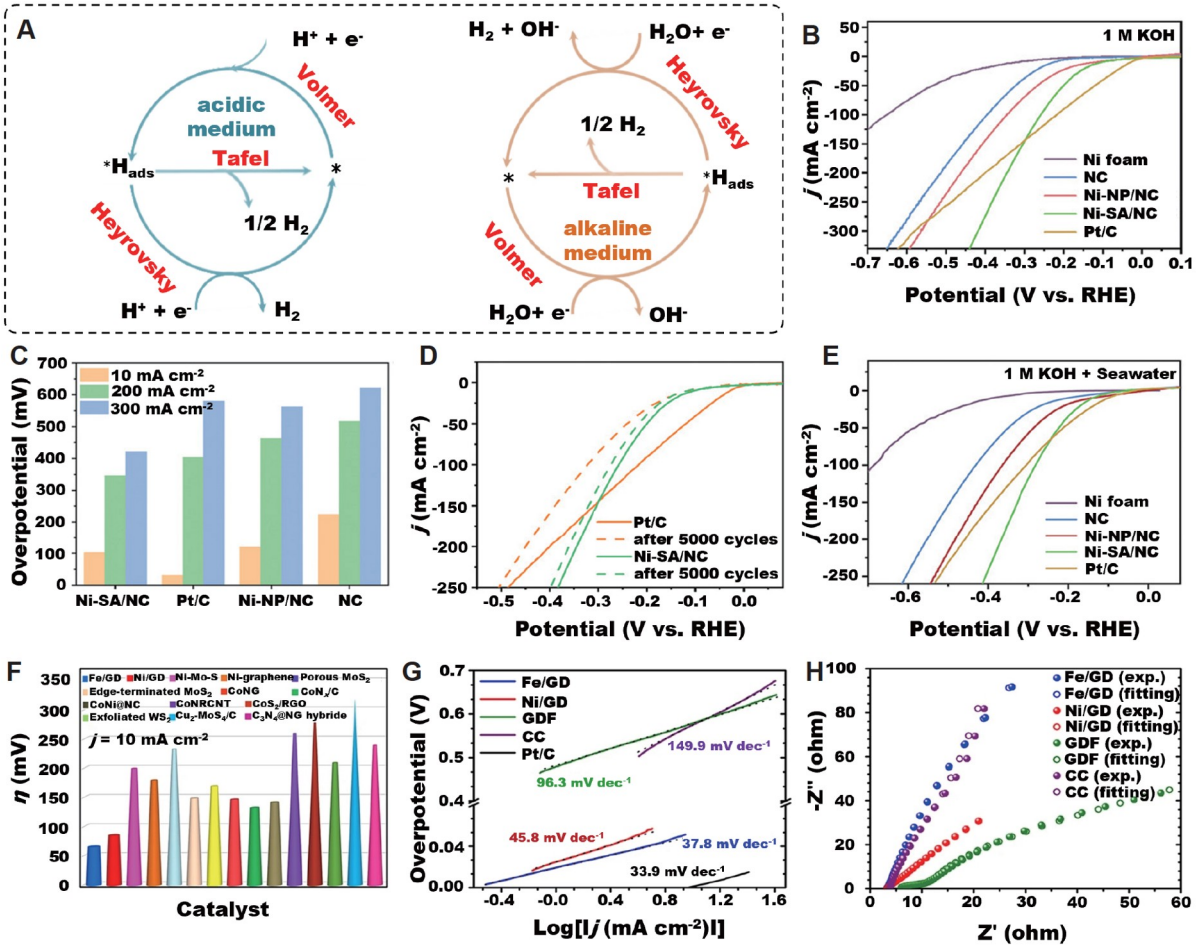

Figure 16 NPM-SACs/CS for HER. (A) The proposed catalytic pathways for hydrogen release in an acidic medium or alkaline medium, where * represents the active site. (B) Linear sweep voltammetry (LSV) curves and (C) overpotentials at certain current density (j = 10, 200 and 300 mA cm^{-2}) of Ni-SA/NC and control samples in 1 mol L^{-1} KOH. (D) LSV curves of Ni-SA/NC before and after 5000 cycles in 1 mol L^{-1} KOH. (E) LSV curves of Ni-SA/NC and control samples in 1 mol L^{-1} KOH with seawater. Reproduced with permission from ref. [196]. Copyright©2021, John Wiley and Sons. (F) Comparison of HER performance between Fe/GD and other catalysts in the same period. (G) Tafel plots and (H) nyquist plots of Fe/GD and control samples in 0.5 mol L^{-1} H_2SO_4. Reproduced with permission from ref. [197]. Copyright©2018, Springer Nature.

valence Fe anchored on graphdiyne (Fe/GD), showing strong catalytic activity with a small overpotential of 66 mV to deliver 10 mA cm^{-2} in 0.5 mol L^{-1} H_2SO_4, which was far beyond other HER catalysts of the same period (Figure 16F). Tafel slopes and electrochemical impedance spectroscopy (EIS) revealed that the outstanding performance resulted from the fast reaction kinetics from the Volmer-Tafel path and charge transfer rates from carbon support (Figures 16G and 16H).

OER

Different from HER, OER, as the anodic half-reaction of water electrolysis, undergoes a complicated four-electron transfer process to achieve the release of oxygen [198]. Moreover, in an acidic medium, H_2O acts as an oxygen source; while in an alkaline medium, OH^- serves as an oxygen source. Along with the transfer of

electrons, some adsorption intermediates are continuously produced, such as the OH_{ads} after the first electron transfer, the O_{ads} after the second electron transfer, and the OOH_{ads} after the third electron transfer (Figure 17A). Some hypotheses suggest that the self-combination of O_{ads} may directly generate O_2 without the additional two-step electron transfer process, but so far few suitable catalysts can overcome the extremely powerful barrier caused by the self-combination of O_{ads}. For the OER process, a smaller Tafel slope indicates that the rate-limiting step is at the end of the multi-electron transfer reaction, which is usually a sign of a good electrocatalyst.

Although the performance of the reported OER catalysts has been comparable to or even exceeded the traditional noble metal oxide materials, the catalytic activity and mechanism of OER still need to be further explored and developed. Zhang *et al*. [199] constructed a Fe SAC ($Fe_1(OH)_x$/P-C) to accelerate the rate-limiting step, namely the formation of OOH_{ads}, where the original Fe^{3+} inactive site was *in situ* conversed into

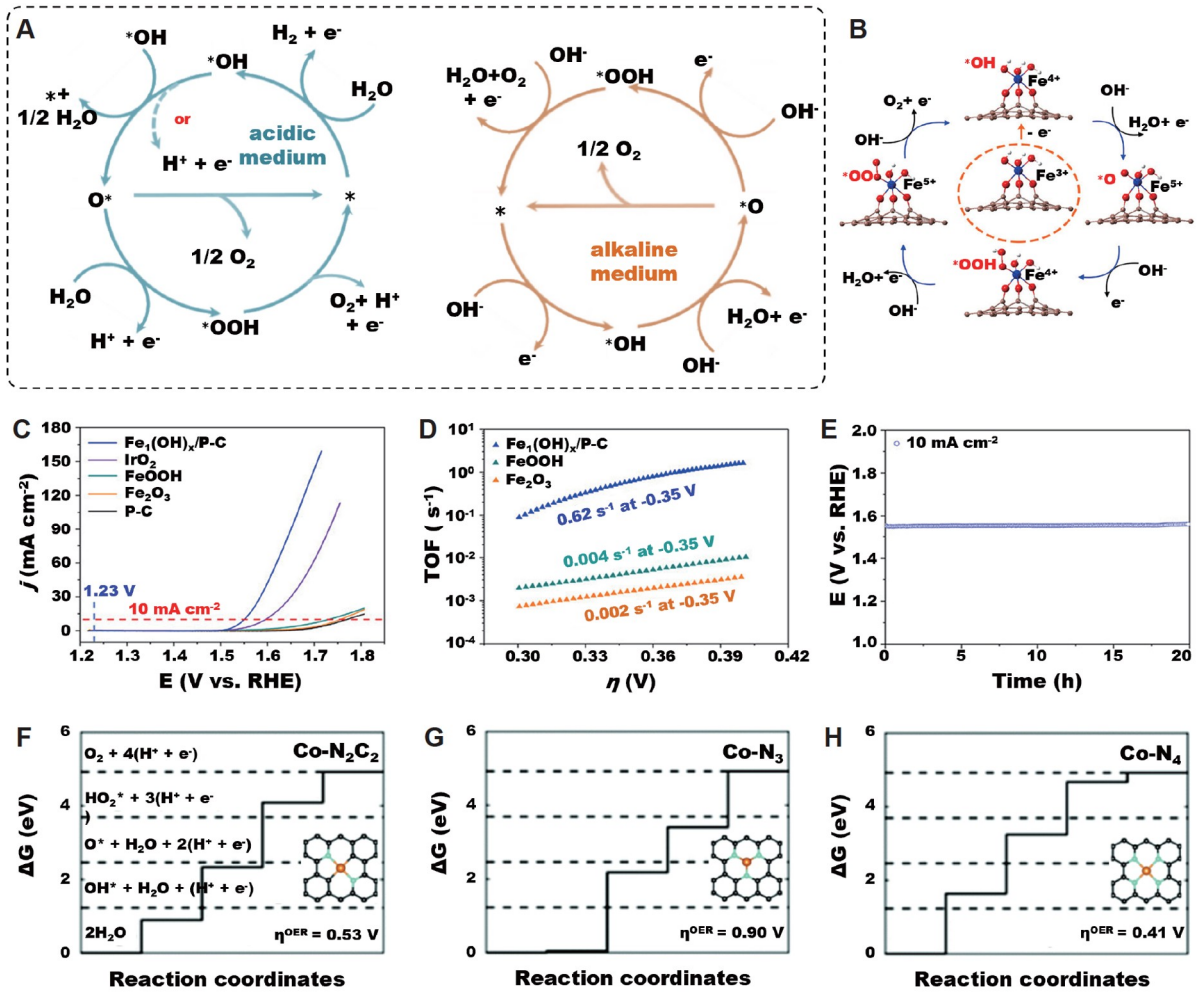

Figure 17 NPM-SACs/CS for OER. (A) The proposed catalytic pathways for oxygen release in an acidic medium or alkaline medium, where * represents the active site. (B) OER reaction mechanism on $Fe_1(OH)_x$/P-C. The blue, brown, red, and white balls represent Fe, C, O, and H atoms, respectively. (C) LSV curves and (D) TOF at the overpotential of 0.35 V of $Fe_1(OH)_x$/P-C and control samples in 1.0 mol L^{-1} KOH. (E) Chronopotentiometric curve of $Fe_1(OH)_x$/P-C at 10 mA cm^{-2} in 1.0 mol L^{-1} KOH. Reproduced with permission from ref. [199]. Copyright©2021, American Chemical Society. Ball-and-stick model and free energy of (F) Co-N_2C_2, (G) Co-N_3 and (H) Co-N_4. Reproduced with permission from ref. [164]. Copyright©2020, Royal Society of Chemistry.

the real Fe^{4+} active site before the catalytic process (Figure 17B). The excellent OER performance of this Fe SAC was digitized as a low overpotential of 320 mV at 10 mA cm^{-2}, an ultrahigh turnover frequency (TOF) of 0.62 s^{-1} at the overpotential of 0.35 V, and long-term catalytic durability over 20 h in 1.0 mol L^{-1} KOH (Figures 17C–17E). Zhang *et al*. [164] dispersed Co single atom in nitrogen-doped graphene to obtain the specific catalyst of 0.7-Co@NG-750 with desirable OER catalytic performance in both 0.1 and 1.0 mol L^{-1} KOH, which may relate to the existence of Co-N_2C_2 or Co-N_4 active sites according to DFT calculation (Figures 17F–17H).

ORR

Electrochemical oxygen reduction reaction (ORR) is a key reaction in many applications such as fuel cells, metal-air batteries, and the production of hydrogen peroxide [155,200,201]. The ORR is a multi-step electron-transfer reaction, which involves the adsorption of O_2, activation of O–O bond, and the formation of oxygen-containing groups of *OOH, *O, and *OH depending on the reaction pathways [202]. Two-electron-transfer reaction pathway leads to the production of hydrogen peroxide with only *OOH as the reaction intermediate. For a complete four-electron transfer-reaction pathway, associative and dissociative mechanisms are taken into account. The first mechanism involves three reaction intermediates of *OOH, *O, and *OH, while the latter just refers to two reaction intermediates of *O and *OH. Anyway, these multi-step electron-transfer reactions involved in the ORR result in considerably sluggish kinetics. Thus, catalysts are highly required to boost the electrocatalytic activity and selectivity in the attempt to satisfy the needs of energy devices and chemical production techniques. NPM-SACs/CS are widely used as high-efficiency electrocatalysts in the ORR field for energy conversion [203–207]. Great progress has been made in recent years, mainly focusing on single-atom metal active centers and coordination environments to realize high efficiency and selectivity [208,209].

In the beginning, atomically dispersed Fe/Co-N-C catalysts are widely studied possibly because they are relatively easily realized just by using the mature processing technique of traditional Fe/Co-N-C materials for reference. For example, Sa *et al*. [210] proposed a silica-protective-layer-assisted strategy to suppress the formation of Fe nanoparticles, resulting in the Fe-N_4 active sites enriched in the atomically dispersed Fe-N-C catalyst (Figure 18A). Benefiting from high-activity and high-density Fe-N_4 sites, excellent fuel cell performances (peak power density: 380 mW cm^{-2} for alkaline anion exchange membrane fuel cell while 580 mW cm^{-2} for proton exchange membrane fuel cell) were achieved when the final Fe-N-C catalyst was used as the cathodic electrocatalyst (Figures 18B and 18C). Soon afterward, lots of preparation methods have been developed to achieve atomically dispersed Fe/Co-N-C catalysts with a high concentration of Fe/Co-N_4, such as the atomic isolation method [211–213], MOFs derived way [214–216], additive-assisted strategy [217–219], and confine method [220–222], with the attempt to realize highly efficient four-electron-transfer ORR pathway for meeting the application requirements of energy devices. Meanwhile, all kinds of new-type single-atom metal (Cu, Mn, Ce, Zn, etc.) catalysts have been reported, showing a relatively low overpotential for four-electron-transfer ORR performance [96,223–225]. In addition, by virtue of regulating the coordination environments to optimize the electronic structure of metal centers, four-electron-transfer ORR activity can be improved or the corresponding ORR mechanism can be completely changed [226–228]. For instance, Gong *et al*. [229] reported that low-coordinated Co-N_2 moiety is efficient for the two-electron-

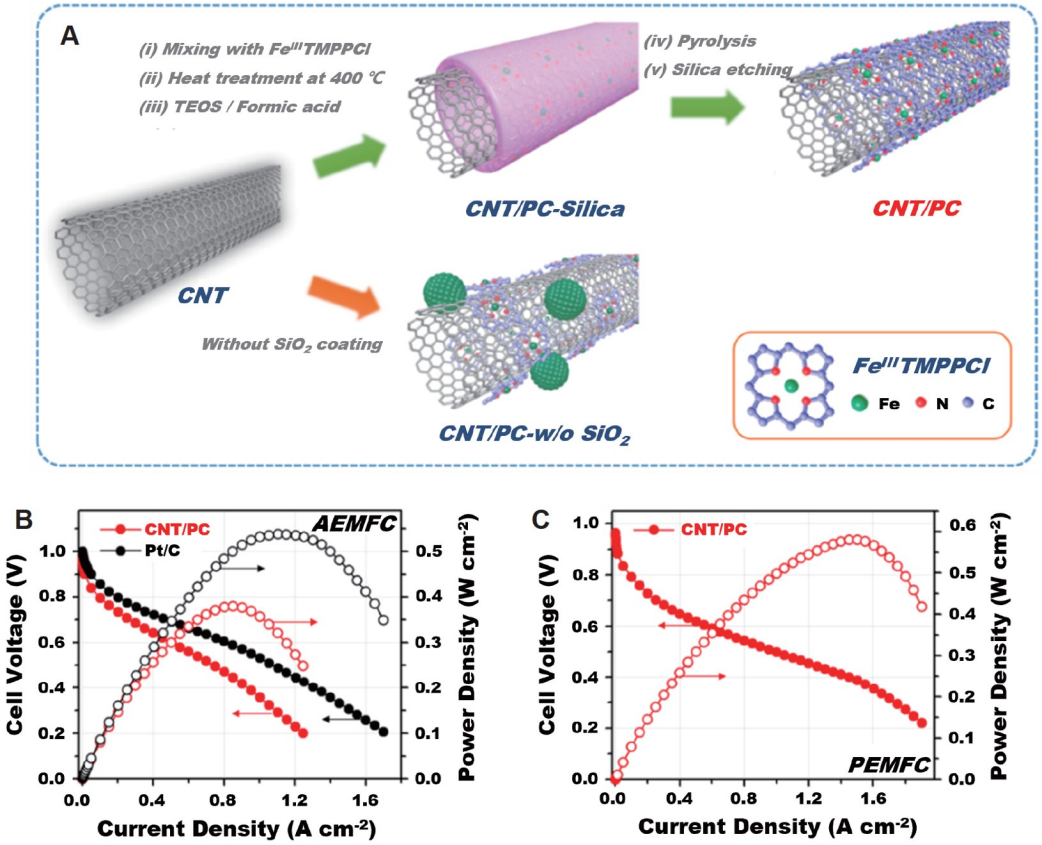

Figure 18 NPM-SACs/CS for ORR. (A) Synthetic scheme for the preparation of CNT/PC catalysts. (B) Alkaline AEMFC performances of MEAs using CNT/PC and Pt/C as cathode catalysts. (C) Acidic PEMFC performance of CNT/PC-based MEA. Reproduced with permission from ref. [210]. Copyright©2016, American Chemical Society.

transfer product of hydrogen peroxide. Readers can achieve more details about the effect of coordination environments on the ORR activity and selectivity of single-atom metal catalysts from the specialized reviews [230].

NRR

Ammonia (NH_3) is a crucial raw material for the synthesis of agricultural fertilizers and fiber fields. It also acts as a clean alternative fuel and hydrogen carrier for storage and delivery [231,232]. Currently, the industrial synthesis of NH_3 heavily depends on the traditional Haber-Bosch method with harsh conditions, consuming 1%–2% of the global energy supply annually. Moreover, this process is not environmentally friendly [233]. Electrocatalytic nitrogen reduction reaction (NRR) is a very attractive and sustainable strategy to convert water and N_2 to NH_3 under ambient conditions using renewable electricity. However, efficient e-NRR has been confirmed to be extremely challenging in practice because of the large amount of energy required to break nonpolar triple bonds. Furthermore, since the theoretical potential of HER is lower than that of NRR, HER is always a strong competing process in NRR [221,234,235]. The electrocatalyst plays an important role in the performance of NRR [236]. Therefore, it is very significant to develop novel electrocatalysts to overcome the challenging issues for the practical application of NRR in the industry.

NPM-SACs/CS show great potential application toward NRR due to the abundant exposed active sites and high catalytic activity [237]. For example, Han and co-workers [238] synthesized single Mo atoms anchored on N-doped porous carbon as low-cost catalysts for NRR (Figure 19A). Benefitting from the hierarchical porous frameworks and the highly exposed active sites, the prepared catalyst showed a high NH_3 yield rate of 34.0 μg h^{-1} $mgcat^{-1}$, as well as a high FE of 14.6% in 0.1 mol L^{-1} KOH (Figure 19B). Similarly, atomically dispersed Ni deposited on N-doped carbon achieved a high NH_3 FE of 21.0% at −0.2 V under alkaline conditions. The DFT calculation revealed that the Ni-N_3 sites were mainly responsible for the experimentally observed activity and selectivity [239]. Recently, Wang *et al*. [240] also demonstrate that under ambient conditions, Fe-SAC on N-doped carbon could make the ammonia synthesis process to a significant Faradaic efficiency of 56.55% with an onset potential of 0.193 V (Figures 19C and 19D). The reliability of the NH_3 production data was determined by an N^{15} isotopic labeling experiment. And the molecular dynamics simulations as well as the first-principle calculations also demonstrated a small energy barrier for N_2 access to the single-atom iron sites, which benefits preferential N_2 adsorption instead of H adsorption (Figure 19E).

Conclusions and outlook

NPM-SACs/CS, as a new type of catalyst, have shown great application prospects for many energy-conversion applications, such as CO_2RR, HER, OER, ORR, and NRR. At present, NPM-SACs/CS have been

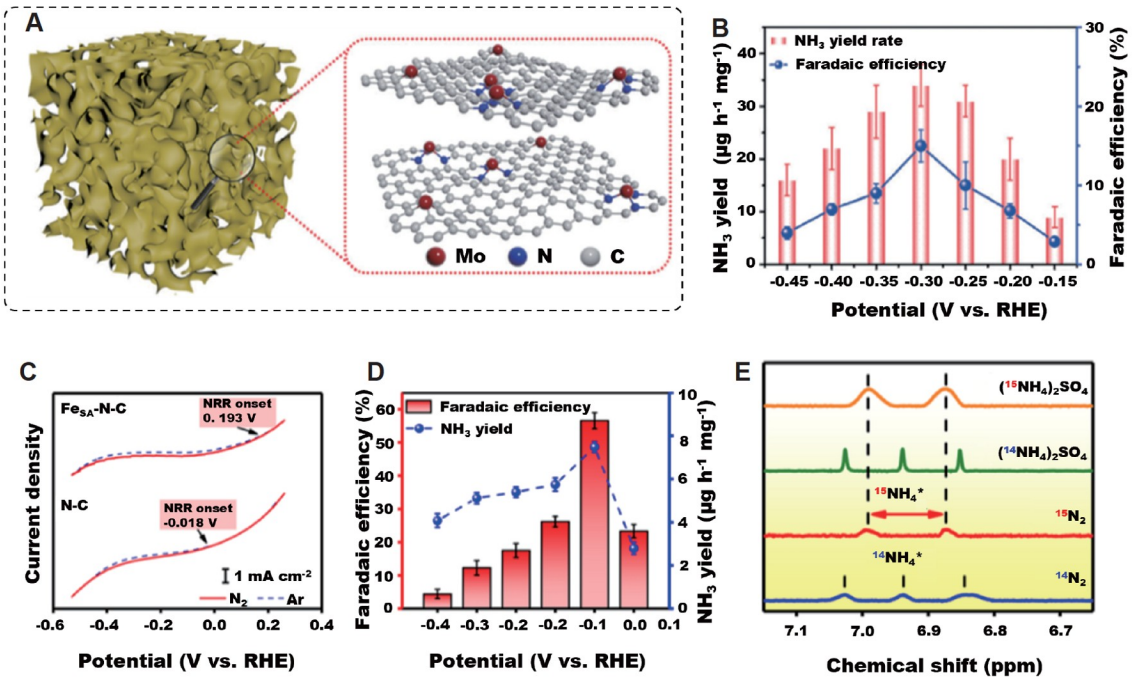

Figure 19 NPM-SACs/CS for NRR. (A) An illustration of SA-Mo/NPC and its corresponding atomic structure model. (B) NH_3 yield rate (red) and FE (blue) at each given potential. Reproduced with permission from ref. [238]. Copyright©2019, John Wiley and Sons. (C) Linear sweep voltammograms of single-atom dispersed Fe-N-C (Fe SA-N-C) and nitrogen-doped carbon (N-C) in Ar-saturated (dashed line) or N_2-saturated (solid line) 0.1 mol L^{-1} KOH solution with a scan rate of 50 mV s^{-1}. (D) NH_3 Faradaic efficiencies and mass-normalized yield rates at each given potential of Fe SA-N-C. (E) N^{15} isotope labeling experiment. Reproduced with permission from ref. [240]. Copyright©2019, Springer Nature.

successfully prepared by many methods, like high-temperature pyrolysis, physical and chemical deposition, impregnation adsorption, ball milling, and ultrafast synthesis. To precisely identify the atom and electronic structure of NPM-SACs/CS, many advanced characterization techniques have been developed. Furthermore, to obtain the high performance of NPM-SACs/CS, various structural tuning strategies are also discussed here. Last, we also summarize the recent studies of NPM-SACs/CS in energy conversion applications. Over the past few decades, some headway has been made in promoting the catalytic performance of NPM-SACs/CS. However, the NPM-SACs/CS still have many challenges before practical application. A few key challenges are as follows.

Firstly, control synthesis of high metal loading NPM-SACs/CS remains intractable. For instance, to reach high electrical conductivity in carbon support, high-temperature treatment for graphitizing the carbon precursors usually is needed, which was beneficial for electrocatalytic applications. However, if there is no strong interaction between the metal atoms and the carbon substrates, the aggregation and sintering of metal atoms into nanoclusters or nanoparticles would often happen. This phenomenon usually alters the electronic structure and reduces the number of active sites, thus decreasing the catalytic performance of NPM-SACs/CS. Although newly-developed ultrafast synthesis, like microwave heating and laser radiation, could shorten the exposure time to extreme heating conditions, rapid monitoring and accurate control of reaction temperature remain challenges. Therefore, it is meaningful to develop novel methods to prepare high metal loading with superior catalytic performance for energy conversion.

Secondly, the identification of single atoms relies on advanced characterization techniques. So far, the XAS technique has been mainly used to identify the coordination environments of NPM-SACs/CS. However, this technique just offers bulk average information due to its bulk-sensitive properties. Thus, further exploration of new characterization technology with a high spatial resolution is extremely critical. Moreover, it is important to combine *in situ* characterization techniques to confirm the actual active sites of NPM-SACs/CS and their dynamic variation over the reaction process, as it is closely related to the internal activity.

Thirdly, due to the electronic and geometric structure of the central metal atom being mainly affected by the coordination environment, exploring new coordination environments may boost the catalytic performances of the NPM-SACs/CS. The common strategy to tune coordination environments is introducing heteroatomic doping (N, S, O, P, etc.). Thus, studies of other elements (Te, Se) as coordination atoms may exhibit an unexpected catalytic effect. Besides, it is imperative to study the location of bimetallic center or polymetallic center sites for achieving superior performance because of the asymmetric distribution of charge. In short, rationally adjusting the coordination structure of NPM-SACs/CS for designing highly active catalysts is important for energy conversion electrocatalysis.

Fourthly, the structure-activity relationship of NPM-SACs/CS for electrochemical reactions is still in the early exploratory stage. Theoretical simulation is helpful to understand the structure-activity relationship of NPM-SACs/CS at the atomic level. At present, DFT calculation is an extremely useful tool to explore the structural characteristics and speculate the catalytic path by providing the adsorption energies of the intermediates and the reaction-free energy of each step. However, in order to bring the theoretical model and reaction mechanism closer to reality, more accurate models should be exploited. Furthermore, we believe that a clever combination of DFT calculation and machine learning can accelerate the development of single-atom electrocatalysts and deepen people's understanding of single-atom catalysts.

Finally, exploring the stability of SACs under reaction conditions is also vital for the development of

single-atom catalysis in the electrochemical fields. Despite huge advances in the development of SACs, the overall detection and characterization of loaded SACs after the reaction is still lacking. The comprehensive characterizations of the overwhelming majority of the existing literature are restricted to the experimental conditions before reactions. This may be due to the scarce availability of advanced *in situ* characterization methods. Nevertheless, carefully characterizing and studying the sample after the reaction with the help of the *in situ* characterization technique, would go a long way to revealing the precise activity of SACs [241]. There would be thorny questions that need to be solved, like the stability of the support skeleton, the interaction of the coordinated atoms with the central metal atoms, and surface poisoning caused by the products or intermediates under the reaction conditions. In the future, more studies in this regard would ensure improvements to reveal the precise active sites and the underlying reaction mechanism of the specific reactions.

Data availability

The original data are available from the corresponding authors upon reasonable request.

Funding

L.X.L. would like to thank the support from the China Postdoctoral Science Foundation (2022M711553). Y.W. would like to acknowledge the support from the National Natural Science Foundation of China (22171132), the Innovation Fund from Nanjing University (020514913419), the Program for Innovative Talents and Entrepreneurs in Jiangsu (020513006012 and 020513006014), and the National Key R&D Program of China (2002YFB3607000). W.Z. would like to acknowledge the support from the National Natural Science Foundation of China (22176086), Natural Science Foundation of Jiangsu Province (BK20210189), State Key Laboratory of Pollution Control and Resource Reuse (PCRR-ZZ-202106), the Fundamental Research Funds for the Central Universities (021114380183, 021114380189 and 021114380199), the Research Funds from the Nanjing Science and Technology Innovation Project for Chinese Scholars Studying Abroad (13006003), the Research Funds from Frontiers Science Center for Critical Earth Material Cycling of Nanjing University, and Research Funds for Jiangsu Distinguished Professor. Y.L. would like to thank the support from the Washington State University startup fund.

Author contributions

LX.L., Y.D., Z.L., J.L., D.D., F.L., Y.W., W.Z. and Y.L. designed the entire study and wrote the manuscript with input from all of the authors. H.D., L.Z. and X.L. executed the data collection and analyses. All of the authors read and approved the final manuscript.

Conflict of interest

The authors declare no conflict of interest.

References

1 Zhu C, Fu S, Shi Q, *et al.* Single-atom electrocatalysts. *Angew Chem Int Ed* 2017; **56**: 13944–13960.

2 Fei H, Dong J, Chen D, *et al.* Single atom electrocatalysts supported on graphene or graphene-like carbons. *Chem Soc Rev* 2019; **48**: 5207–5241.

3 Dou X, Wang Y, Ciais P, *et al*. Near-real-time global gridded daily CO_2 emissions. *Innovation* 2022; **3**: 100182.

4 Zhao Q, Yu P, Mahendran R, *et al.* Global climate change and human health: Pathways and possible solutions. *Eco-Environ Health* 2022; **1**: 53–62.

5 Salemdeeb R, Saint R, Clark W, *et al*. A pragmatic and industry-oriented framework for data quality assessment of environmental footprint tools. *Resour Environ Sust* 2021; **3**: 100019.

6 Yuan Y, Lu J. Demanding energy from carbon. *Carbon Energy* 2019; **1**: 8–12.

7 Chai Y, Lyu Z, Du H, *et al.* Recent progress on rational design of catalysts for fermentative hydrogen production. *SusMat* 2022; **2**: 392–410.

8 Chen JM. Carbon neutrality: Toward a sustainable future. *Innovation* 2021; **2**: 100127.

9 Fu J, Li P, Lin Y, *et al.* Fight for carbon neutrality with state-of-the-art negative carbon emission technologies. *Eco-Environ Health* 2022; **1**: 259–279.

10 Zhu W, Tackett BM, Chen JG, *et al.* Bimetallic electrocatalysts for CO_2 reduction. *Top Curr Chem (Z)* 2018; **376**: 41.

11 Wang X, Li P, Cao Y, *et al*. Techno-economic analysis and industrial application prospects of single-atom materials in CO_2 catalysis. *Chem J Chin U* 2022; **43**: 20220347.

12 Li D, Park EJ, Zhu W, *et al.* Highly quaternized polystyrene ionomers for high performance anion exchange membrane water electrolysers. *Nat Energy* 2020; **5**: 378–385.

13 Lv H, Xi Z, Chen Z, *et al.* A new core/shell NiAu/Au nanoparticle catalyst with Pt-like activity for hydrogen evolution reaction. *J Am Chem Soc* 2015; **137**: 5859–5862.

14 Tian H, Zhu W, Shi Q, *et al.* Bimetallic Ir_xPb nanowire networks with enhanced electrocatalytic activity for the oxygen evolution reaction. *J Mater Chem A* 2022; **10**: 11196–11204.

15 Shi Q, Zhu C, Du D, *et al.* Robust noble metal-based electrocatalysts for oxygen evolution reaction. *Chem Soc Rev* 2019; **48**: 3181–3192.

16 Shi Q, Fu S, Zhu C, *et al.* Metal-organic frameworks-based catalysts for electrochemical oxygen evolution. *Mater Horiz* 2019; **6**: 684–702.

17 Guo S, Zhang X, Zhu W, *et al.* Nanocatalyst superior to Pt for oxygen reduction reactions: The case of core/shell Ag (Au)/CuPd nanoparticles. *J Am Chem Soc* 2014; **136**: 15026–15033.

18 Wei X, Luo X, Wu N, *et al.* Recent advances in synergistically enhanced single-atomic site catalysts for boosted oxygen reduction reaction. *Nano Energy* 2021; **84**: 105817.

19 Ding S, Lyu Z, Sarnello E, *et al.* A MnO_x enhanced atomically dispersed iron-nitrogen-carbon catalyst for the oxygen reduction reaction. *J Mater Chem A* 2022; **10**: 5981–5989.

20 Ding S, Barr JA, Shi Q, *et al.* Engineering atomic single metal-FeN_4Cl sites with enhanced oxygen-reduction activity for high-performance proton exchange membrane fuel cells. *ACS Nano* 2022; **16**: 15165–15174.

21 Yan D, Li H, Chen C, *et al.* Defect engineering strategies for nitrogen reduction reactions under ambient conditions. *Small Methods* 2018; **3**: 1800331.

22 Yang Y, Yang Y, Pei Z, *et al.* Recent progress of carbon-supported single-atom catalysts for energy conversion and storage. *Matter* 2020; **3**: 1442–1476.

23 Wan Y, Xu J, Lv R. Heterogeneous electrocatalysts design for nitrogen reduction reaction under ambient conditions. *Mater Today* 2019; **27**: 69–90.

24 Copéret C, Chabanas M, Petroff Saint-Arroman R, *et al.* Homogeneous and heterogeneous catalysis: Bridging the gap through surface organometallic chemistry. *Angew Chem Int Ed* 2003; **42**: 156–181.

25 Zhu C, Shi Q, Feng S, *et al.* Single-atom catalysts for electrochemical water splitting. *ACS Energy Lett* 2018; **3**: 1713–1721.

26 Wang A, Li J, Zhang T. Heterogeneous single-atom catalysis. *Nat Rev Chem* 2018; **2**: 65–81.

27 Liu J. Catalysis by supported single metal atoms. *ACS Catal* 2017; **7**: 34–59.

28 Wu J, Xiong L, Zhao B, *et al.* Densely populated single atom catalysts. *Small Methods* 2020; **4**: 1900540.

29 Qiao B, Wang A, Yang X, *et al.* Single-atom catalysis of CO oxidation using Pt_1/FeO_x. *Nat Chem* 2011; **3**: 634–641.

30 Yang XF, Wang A, Qiao B, *et al.* Single-atom catalysts: A new frontier in heterogeneous catalysis. *Acc Chem Res* 2013; **46**: 1740–1748.

31 Lin J, Wang A, Qiao B, *et al.* Remarkable performance of Ir_1/FeO_x single-atom catalyst in water gas shift reaction. *J*

Am Chem Soc 2013; **135**: 15314–15317.

32 Wang YG, Mei D, Glezakou VA, *et al.* Dynamic formation of single-atom catalytic active sites on ceria-supported gold nanoparticles. *Nat Commun* 2015; **6**: 6511.

33 Liu JC, Wang YG, Li J. Toward rational design of oxide-supported single-atom catalysts: Atomic dispersion of gold on ceria. *J Am Chem Soc* 2017; **139**: 6190–6199.

34 Wei S, Li A, Liu JC, *et al.* Direct observation of noble metal nanoparticles transforming to thermally stable single atoms. *Nat Nanotech* 2018; **13**: 856–861.

35 Lang R, Xi W, Liu JC, *et al.* Non defect-stabilized thermally stable single-atom catalyst. *Nat Commun* 2019; **10**: 234.

36 Ren Y, Tang Y, Zhang L, *et al.* Unraveling the coordination structure-performance relationship in Pt_1/Fe_2O_3 single-atom catalyst. *Nat Commun* 2019; **10**: 4500.

37 Taylor HS. A theory of the catalytic surface. *Proc R Soc Lond A* 1925; **108**: 105–111.

38 Rooney JJ, Webb G. The importance of π-bonded intermediates in hydrocarbon reactions on transition metal catalysts. *J Catal* 1964; **3**: 488–501.

39 Asakura K, Nagahiro H, Ichikuni N, *et al.* Structure and catalytic combustion activity of atomically dispersed Pt species at MgO surface. *Appl Catal A-Gen* 1999; **188**: 313–324.

40 Fu Q, Saltsburg H, Flytzani-Stephanopoulos M. Active nonmetallic Au and Pt species on ceria-based water-gas shift catalysts. *Science*, 2003; **301**: 935–938.

41 Zhang X, Shi H, Xu BQ. Catalysis by gold: Isolated surface Au^{3+} ions are active sites for selective hydrogenation of 1,3-butadiene over Au/ZrO_2 catalysts. *Angew Chem Int Ed* 2005; **44**: 7132–7135.

42 Hackett S, Brydson R, Gass M, *et al.* High-activity, single-site mesoporous Pd/Al_2O_3 catalysts for selective aerobic oxidation of allylic alcohols. *Angew Chem Int Ed* 2007; **46**: 8593–8596.

43 Zhang N, Li L, Huang X, *et al*. Research progress of single-atom catalysis. *J Chin Soc Rare Earths* 2018; 36: 513–532.

44 Nie L, Mei D, Xiong H, *et al.* Activation of surface lattice oxygen in single-atom Pt/CeO_2 for low-temperature CO oxidation. *Science* 2017; **358**: 1419–1423.

45 Gu J, Jian M, Huang L, *et al.* Synergizing metal-support interactions and spatial confinement boosts dynamics of atomic nickel for hydrogenations. *Nat Nanotechnol* 2021; **16**: 1141–1149.

46 Zhu Y, Zhao K, Shi J, *et al.* Strain engineering of a defect-free, single-layer MoS_2 substrate for highly efficient single-atom catalysis of CO oxidation. *ACS Appl Mater Interfaces* 2019; **11**: 32887–32894.

47 Yan J, Kong L, Ji Y, *et al.* Single atom tungsten doped ultrathin α-$Ni(OH)_2$ for enhanced electrocatalytic water oxidation. *Nat Commun* 2019; **10**: 2149.

48 Yang T, Song TT, Zhou J, *et al.* High-throughput screening of transition metal single atom catalysts anchored on molybdenum disulfide for nitrogen fixation. *Nano Energy* 2020; **68**: 104304.

49 Jiang K, Luo M, Peng M, *et al.* Dynamic active-site generation of atomic iridium stabilized on nanoporous metal phosphides for water oxidation. *Nat Commun* 2020; **11**: 2701.

50 Zhao D, Chen Z, Yang W, *et al.* MXene(Ti_3C_2) vacancy-confined single-atom catalyst for efficient functionalization of CO_2. *J Am Chem Soc* 2019; **141**: 4086–4093.

51 Peng W, Luo M, Xu X, *et al.* Spontaneous atomic ruthenium doping in Mo_2CT_X MXene defects enhances electrocatalytic activity for the nitrogen reduction reaction. *Adv Energy Mater* 2020; **10**: 2001364.

52 Cheng Y, Dai J, Song Y, *et al.* Single molybdenum atom anchored on 2D Ti_2NO_2 MXene as a promising electrocatalyst for N_2 fixation. *Nanoscale* 2019; **11**: 18132–18141.

53 Wu Y, Jiao L, Luo X, *et al*. Oxidase-like Fe-N-C single-atom nanozymes for the detection of acetylcholinesterase activity. *Small* 2019; **15**: e1903108.

54 Xu H, Zhao Y, Wang Q, *et al.* Supports promote single-atom catalysts toward advanced electrocatalysis. *Coord Chem Rev* 2022; **451**: 214261.

55 Jiao L, Xu W, Yan H, *et al.* Fe-N-C single-atom nanozymes for the intracellular hydrogen peroxide detection. *Anal Chem* 2019; **91**: 11994–11999.

56 Li X, Fan L, Xu B, *et al.* Single-atom-like B-N_3 sites in ordered macroporous carbon for efficient oxygen reduction reaction. *ACS Appl Mater Interfaces* 2021; **13**: 53892–53903.

57 Bisen OY, Yadav AK, Nanda KK. Self-organized single-atom tungsten supported on the N-doped carbon matrix for durable oxygen reduction. *ACS Appl Mater Interfaces* 2020; **12**: 43586–43595.

58 Guo J, Huo J, Liu Y, *et al.* Nitrogen-doped porous carbon supported nonprecious metal single-atom electrocatalysts: From synthesis to application. *Small Methods* 2019; **3**: 1900159.

59 Wang T, Zhao Q, Fu Y, *et al.* Carbon-rich nonprecious metal single atom electrocatalysts for CO_2 reduction and hydrogen evolution. *Small Methods* 2019; **3**: 1900210.

60 Peng Y, Lu B, Chen S. Carbon-supported single atom catalysts for electrochemical energy conversion and storage. *Adv Mater* 2018; **30**: 1801995.

61 Wang M, Wu Y, Li X, *et al.* Achieving a highly efficient oxygen reduction reaction *via* a molecular Fe single atom catalyst. *Nanoscale* 2022; **14**: 8255–8259.

62 Liu K, Fu J, Zhu L, *et al.* Single-atom transition metals supported on black phosphorene for electrochemical nitrogen reduction. *Nanoscale* 2020; **12**: 4903–4908.

63 Zhang Q, Guan J. Single-atom catalysts for electrocatalytic applications. *Adv Funct Mater* 2020; **30**: 2000768.

64 Shi Q, Zhu W, Zhong H, *et al.* Highly dispersed platinum atoms on the surface of AuCu metallic aerogels for enabling H_2O_2 production. *ACS Appl Energy Mater* 2019; **2**: 7722–7727.

65 Jiang M, Wang F, Yang F, *et al.* Rationalization on high-loading iron and cobalt dual metal single atoms and mechanistic insight into the oxygen reduction reaction. *Nano Energy* 2022; **93**: 106793.

66 Song X, Li N, Zhang H, *et al.* Graphene-supported single nickel atom catalyst for highly selective and efficient hydrogen peroxide production. *ACS Appl Mater Interfaces* 2020; **12**: 17519–17527.

67 Li P, Zhao G, Cui P, *et al.* Nickel single atom-decorated carbon nanosheets as multifunctional electrocatalyst supports toward efficient alkaline hydrogen evolution. *Nano Energy* 2021; **83**: 105850.

68 Li Q, Chen W, Xiao H, *et al.* Fe isolated single atoms on S, N codoped carbon by copolymer pyrolysis strategy for highly efficient oxygen reduction reaction. *Adv Mater* 2018; **30**: 1800588.

69 Pan Y, Liu S, Sun K, *et al.* A bimetallic Zn/Fe polyphthalocyanine-derived single-atom Fe-N_4 catalytic site: A superior trifunctional catalyst for overall water splitting and Zn-air batteries. *Angew Chem Int Ed* 2018; **57**: 8614–8618.

70 Cai Y, Fu J, Zhou Y, *et al.* Insights on forming N,O-coordinated Cu single-atom catalysts for electrochemical reduction CO_2 to methane. *Nat Commun* 2021; **12**: 586.

71 Zhang Z, Gao X, Dou M, *et al.* Biomass derived N-doped porous carbon supported single Fe atoms as superior electrocatalysts for oxygen reduction. *Small* 2017; **13**: 1604290.

72 Wang Y, Shi R, Shang L, *et al.* High-efficiency oxygen reduction to hydrogen peroxide catalyzed by nickel single-atom catalysts with tetradentate N_2O_2 coordination in a three-phase flow cell. *Angew Chem Int Ed* 2020; **59**: 13057–13062.

73 Sun Q, Ren W, Zhao Y, *et al.* Gram-scale synthesis of single-atom metal-N-CNT catalysts for highly efficient CO_2 electroreduction. *Chem Commun* 2021; **57**: 1514–1517.

74 Jiang K, Siahrostami S, Zheng T, *et al.* Isolated Ni single atoms in graphene nanosheets for high-performance CO_2 reduction. *Energy Environ Sci* 2018; **11**: 893–903.

75 Fu S, Zhu C, Su D, *et al.* Porous carbon-hosted atomically dispersed iron-nitrogen moiety as enhanced electrocatalysts for oxygen reduction reaction in a wide range of pH. *Small* 2018; **14**: 1703118.

76 Al-Zoubi T, Zhou Y, Yin X, *et al.* Preparation of nonprecious metal electrocatalysts for the reduction of oxygen using a low-temperature sacrificial metal. *J Am Chem Soc* 2020; **142**: 5477–5481.

77 Xie X, Peng L, Yang H, *et al.* MIL-101-derived mesoporous carbon supporting highly exposed Fe single-atom sites as efficient oxygen reduction reaction catalysts. *Adv Mater* 2021; **33**: 2101038.

78 Zhu C, Shi Q, Xu BZ, *et al.* Hierarchically porous M-N-C (M = Co and Fe) single-atom electrocatalysts with robust MN_x active moieties enable enhanced ORR performance. *Adv Energy Mater* 2018; **8**: 1801956.

79 Huang M, Deng B, Zhao X, *et al.* Template-sacrificing synthesis of well-defined asymmetrically coordinated single-

atom catalysts for highly efficient CO_2 electrocatalytic reduction. *ACS Nano* 2022; **16**: 2110–2119.

80 Liu W, Zhang L, Liu X, *et al.* Discriminating catalytically active FeN_x species of atomically dispersed Fe-N-C catalyst for selective oxidation of the C–H bond. *J Am Chem Soc* 2017; **139**: 10790–10798.

81 Liu W, Zhang L, Yan W, *et al.* Single-atom dispersed Co-N-C catalyst: Structure identification and performance for hydrogenative coupling of nitroarenes. *Chem Sci* 2016; **7**: 5758–5764.

82 Wang M, Yang W, Li X, *et al.* Atomically dispersed Fe-heteroatom (N, S) bridge sites anchored on carbon nanosheets for promoting oxygen reduction reaction. *ACS Energy Lett* 2021; **6**: 379–386.

83 Wang Y, Shi C, Sha J, *et al.* Single-atom cobalt supported on nitrogen-doped three-dimensional carbon facilitating polysulfide conversion in lithium-sulfur batteries. *ACS Appl Mater Interfaces* 2022; **14**: 25337–25347.

84 Cheng N, Stambula S, Wang D, *et al.* Platinum single-atom and cluster catalysis of the hydrogen evolution reaction. *Nat Commun* 2016; **7**: 13638.

85 Song Z, Zhu Y, Liu H, *et al.* Engineering the low coordinated Pt single atom to achieve the superior electrocatalytic performance toward oxygen reduction. *Small* 2020; **16**: 2003096.

86 Zhang L, Wang Q, Si R, *et al.* New insight of pyrrole-like nitrogen for boosting hydrogen evolution activity and stability of Pt single atoms. *Small* 2021; **17**: 2004453.

87 Yan H, Zhao X, Guo N, *et al.* Atomic engineering of high-density isolated Co atoms on graphene with proximal-atom controlled reaction selectivity. *Nat Commun* 2018; **9**: 3197.

88 Cao Y, Chen S, Luo Q, *et al.* Atomic-level insight into optimizing the hydrogen evolution pathway over a Co_1-N_4 single-site photocatalyst. *Angew Chem Int Ed* 2017; **56**: 12191–12196.

89 Swain S, Altaee A, Saxena M, *et al*. A comprehensive study on heterogeneous single atom catalysis: Current progress, and challenges. *Coordin Chem Rev* 2022; 470: 214710.

90 Qiu HJ, Du P, Hu K, *et al.* Metal and nonmetal codoped 3D nanoporous graphene for efficient bifunctional electrocatalysis and rechargeable Zn-air batteries. *Adv Mater* 2019; **31**: 1900843.

91 Li X, Yang X, Liu L, *et al.* Chemical vapor deposition for N/S-doped single Fe site catalysts for the oxygen reduction in direct methanol fuel cells. *ACS Catal* 2021; **11**: 7450–7459.

92 He Y, Li Y, Zhang J, *et al.* Low-temperature strategy toward Ni-NC@Ni core-shell nanostructure with single-Ni sites for efficient CO_2 electroreduction. *Nano Energy* 2020; **77**: 105010.

93 Xu J, Li R, Xu CQ, *et al.* Underpotential-deposition synthesis and in-line electrochemical analysis of single-atom copper electrocatalysts. *Appl Catal B-Environ* 2021; **289**: 120028.

94 Yan B, Song H, Yang G. A facile and green large-scale fabrication of single atom catalysts for high photocatalytic H_2 evolution activity. *Chem Eng J* 2022; **427**: 131795.

95 Ji D, Fan L, Li L, *et al.* Atomically transition metals on self-supported porous carbon flake arrays as binder-free air cathode for wearable zinc-air batteries. *Adv Mater* 2019; **31**: 1808267.

96 Li JC, Qin X, Xiao F, *et al.* Highly dispersive cerium atoms on carbon nanowires as oxygen reduction reaction electrocatalysts for Zn-air batteries. *Nano Lett* 2021; **21**: 4508–4515.

97 Hai X, Xi S, Mitchell S, *et al.* Scalable two-step annealing method for preparing ultra-high-density single-atom catalyst libraries. *Nat Nanotechnol* 2022; **17**: 174–181.

98 Qian K, Chen H, Li W, *et al.* Single-atom Fe catalyst outperforms its homogeneous counterpart for activating peroxymonosulfate to achieve effective degradation of organic contaminants. *Environ Sci Technol* 2021; **55**: 7034–7043.

99 Wang H, Wang X, Pan J, *et al.* Ball-milling induced debonding of surface atoms from metal bulk for construing high-performance dual-site single-atom catalysts. *Angew Chem Int Ed* 2021; **60**: 23154–23158.

100 Yang S, Yu Y, Dou M, *et al.* Two-dimensional conjugated aromatic networks as high-site-density and single-atom electrocatalysts for the oxygen reduction reaction. *Angew Chem Int Ed* 2019; **58**: 14724–14730.

101 Li C, Chen Z, Yi H, *et al.* Polyvinylpyrrolidone-coordinated single-site platinum catalyst exhibits high activity for hydrogen evolution reaction. *Angew Chem Int Ed* 2020; **59**: 15902–15907.

102 Lu X, Guo C, Zhang M, *et al.* Rational design of palladium single-atoms and clusters supported on silicoaluminophosphate-31 by a photochemical route for chemoselective hydrodeoxygenation of vanillin. *Nano Res* 2021; **14**: 4347–4355.

103 Wei H, Huang K, Zhang L, *et al.* Ice melting to release reactants in solution syntheses. *Angew Chem Int Ed* 2018; **57**: 3354–3359.

104 Fu W, Wan J, Zhang H, *et al.* Photoinduced loading of electron-rich Cu single atoms by moderate coordination for hydrogen evolution. *Nat Commun* 2022; **13**: 5496.

105 Yang J, Qiu Z, Zhao C, *et al. In situ* thermal atomization to convert supported nickel nanoparticles into surface-bound nickel single-atom catalysts. *Angew Chem Int Ed* 2018; **57**: 14095–14100.

106 Qu Y, Li Z, Chen W, *et al.* Direct transformation of bulk copper into copper single sites via emitting and trapping of atoms. *Nat Catal* 2018; **1**: 781–786.

107 Yang Z, Chen B, Chen W, *et al.* Directly transforming copper (I) oxide bulk into isolated single-atom copper sites catalyst through gas-transport approach. *Nat Commun* 2019; **10**: 3734.

108 Zhuang Z, Li Y, Yu R, *et al.* Reversely trapping atoms from a perovskite surface for high-performance and durable fuel cell cathodes. *Nat Catal* 2022; **5**: 300–310.

109 Wang P, Ren Y, Wang R, *et al.* Atomically dispersed cobalt catalyst anchored on nitrogen-doped carbon nanosheets for lithium-oxygen batteries. *Nat Commun* 2020; **11**: 1576.

110 Zhang Z, Chen Y, Zhou L, *et al.* The simplest construction of single-site catalysts by the synergism of micropore trapping and nitrogen anchoring. *Nat Commun* 2019; **10**: 1657.

111 He G, Yan M, Gong H, *et al.* Ultrafast synthetic strategies under extreme heating conditions toward single-atom catalysts. *Int J Extrem Manuf* 2022; **4**: 032003.

112 Xi D, Li J, Low J, *et al.* Limiting the uncoordinated N species in M-N_x single-atom catalysts toward electrocatalytic CO_2 reduction in broad voltage range. *Adv Mater* 2022; **34**: 2104090.

113 Fei H, Dong J, Wan C, *et al.* Microwave-assisted rapid synthesis of graphene-supported single atomic metals. *Adv Mater* 2018; **30**: 1802146.

114 Kang S, Jeong YK, Mhin S, *et al.* Pulsed laser confinement of single atomic catalysts on carbon nanotube matrix for enhanced oxygen evolution reaction. *ACS Nano* 2021; **15**: 4416–4428.

115 Jung JY, Jang J, Kim J, *et al.* Flash bottom-up arc synthesis of nanocarbons as a universal route for fabricating single-atom electrocatalysts. *Small Methods* 2021; **5**: 2100239.

116 Kosmala T, Baby A, Lunardon M, *et al.* Operando visualization of the hydrogen evolution reaction with atomic-scale precision at different metal-graphene interfaces. *Nat Catal* 2021; **4**: 850–859.

117 Patera LL, Bianchini F, Africh C, *et al.* Real-time imaging of adatom-promoted graphene growth on nickel. *Science* 2018; **359**: 1243–1246.

118 Chen J, Wang T, Wang X, *et al.* Promoting electrochemical CO_2 reduction via boosting activation of adsorbed intermediates on iron single-atom catalyst. *Adv Funct Mater* 2022; **32**: 2110174.

119 Wang XX, Cullen DA, Pan YT, *et al.* Nitrogen-coordinated single cobalt atom catalysts for oxygen reduction in proton exchange membrane fuel cells. *Adv Mater* 2018; **30**: 1706758.

120 Shang Y, Duan X, Wang S, *et al.* Carbon-based single atom catalyst: Synthesis, characterization, DFT calculations. *Chin Chem Lett* 2022; **33**: 663–673.

121 Pan Y, Lin R, Chen Y, *et al.* Design of single-atom Co-N_5 catalytic site: A robust electrocatalyst for CO_2 reduction with nearly 100% CO selectivity and remarkable stability. *J Am Chem Soc* 2018; **140**: 4218–4221.

122 Zhao L, Zhang Y, Huang LB, *et al.* Cascade anchoring strategy for general mass production of high-loading single-atomic metal-nitrogen catalysts. *Nat Commun* 2019; **10**: 1278.

123 Liang X, Li Z, Xiao H, *et al.* Two types of single-atom FeN_4 and FeN_5 electrocatalytic active centers on N-doped carbon driving high performance of the SA-Fe-NC oxygen reduction reaction catalyst. *Chem Mater* 2021; **33**: 5542–5554.

124 Peng L, Yang J, Yang Y, *et al.* Mesopore-rich Fe-N-C catalyst with FeN_4-O-NC single-atom sites delivers remarkable oxygen reduction reaction performance in alkaline media. *Adv Mater* 2022; **34**: 2202544.

125 Zhu W, Fu J, Liu J, *et al.* Tuning single atom-nanoparticle ratios of Ni-based catalysts for synthesis gas production from CO_2. *Appl Catal B-Environ* 2020; **264**: 118502.

126 Li Y, Lu XF, Xi S, *et al*. Synthesis of N-doped highly graphitic carbon urchin-like hollow structures loaded with single-Ni atoms towards efficient CO_2 electroreduction. *Angew Chem Int Ed* 2022; **61**: e202201491.

127 Wang B, Wang X, Zou J, *et al.* Simple-cubic carbon frameworks with atomically dispersed iron dopants toward high-efficiency oxygen reduction. *Nano Lett* 2017; **17**: 2003–2009.

128 Li P, Jin Z, Fang Z, *et al.* A single-site iron catalyst with preoccupied active centers that achieves selective ammonia electrosynthesis from nitrate. *Energy Environ Sci* 2021; **14**: 3522–3531.

129 Kramm UI, Herrmann-Geppert I, Behrends J, *et al.* On an easy way to prepare metal-nitrogen doped carbon with exclusive presence of MeN_4-type sites active for the ORR. *J Am Chem Soc* 2016; **138**: 635–640.

130 Han J, Zhang S, Li Y, *et al.* Multi-scale promoting effects of lead for palladium catalyzed aerobic oxidative coupling of methylacrolein with methanol. *Catal Sci Technol* 2015; **5**: 2076–2080.

131 Zhang X, Zhang M, Deng Y, *et al.* A stable low-temperature H_2-production catalyst by crowding Pt on α-MoC. *Nature* 2021; **589**: 396–401.

132 Chen S, Li WH, Jiang W, *et al*. MOF encapsulating N-Heterocyclic carbene-ligated copper single-atom site catalyst towards efficient methane electrosynthesis. *Angew Chem Int Ed* 2022; **61**: e202114450.

133 Poerwoprajitno AR, Gloag L, Watt J, *et al.* A single-Pt-atom-on-Ru-nanoparticle electrocatalyst for CO-resilient methanol oxidation. *Nat Catal* 2022; **5**: 231–237.

134 Gong YN, Zhong W, Li Y, *et al.* Regulating photocatalysis by spin-state manipulation of cobalt in covalent organic frameworks. *J Am Chem Soc* 2020; **142**: 16723–16731.

135 Li XF, Li QK, Cheng J, *et al.* Conversion of dinitrogen to ammonia by FeN_3-embedded graphene. *J Am Chem Soc* 2016; **138**: 8706–8709.

136 Han Y, Li QK, Ye K, *et al.* Impact of active site density on oxygen reduction reactions using monodispersed Fe-N-C single-atom catalysts. *ACS Appl Mater Interfaces* 2020; **12**: 15271–15278.

137 Cao S, Wei S, Wei X, *et al.* Can N, S cocoordination promote single atom catalyst performance in CO_2RR? Fe-N_2S_2 porphyrin versus Fe-N_4 porphyrin. *Small* 2021; **17**: 2100949.

138 Jiang K, Siahrostami S, Akey AJ, *et al.* Transition-metal single atoms in a graphene shell as active centers for highly efficient artificial photosynthesis. *Chem* 2017; **3**: 950–960.

139 Liu X, Jiao Y, Zheng Y, *et al.* Building up a picture of the electrocatalytic nitrogen reduction activity of transition metal single-atom catalysts. *J Am Chem Soc* 2019; **141**: 9664–9672.

140 Li K, Zhang S, Zhang X, *et al.* Atomic tuning of single-atom Fe-N-C catalysts with phosphorus for robust electrochemical CO_2 reduction. *Nano Lett* 2022; **22**: 1557–1565.

141 Xu H, Cheng D, Cao D, *et al.* A universal principle for a rational design of single-atom electrocatalysts. *Nat Catal* 2018; **1**: 339–348.

142 Choi C, Back S, Kim NY, *et al.* Suppression of hydrogen evolution reaction in electrochemical N_2 reduction using single-atom catalysts: A computational guideline. *ACS Catal* 2018; **8**: 7517–7525.

143 Yang W, Zhao M, Ding X, *et al.* The effect of coordination environment on the kinetic and thermodynamic stability of single-atom iron catalysts. *Phys Chem Chem Phys* 2020; **22**: 3983–3989.

144 Liu JC, Xiao H, Li J. Constructing high-loading single-atom/cluster catalysts via an electrochemical potential window strategy. *J Am Chem Soc* 2020; **142**: 3375–3383.

145 Qian SJ, Cao H, Chen JW, *et al.* Critical role of explicit inclusion of solvent and electrode potential in the electrochemical description of nitrogen reduction. *ACS Catal* 2022; **12**: 11530–11540.

146 Zhao H, Cao H, Zhang Z, *et al.* Modeling the potential-dependent kinetics of CO_2 electroreduction on single-nickel atom catalysts with explicit solvation. *ACS Catal* 2022; **12**: 11380–11390.

147 Cao H, Zhang Z, Chen JW, *et al.* Potential-dependent free energy relationship in interpreting the electrochemical performance of CO_2 reduction on single atom catalysts. *ACS Catal* 2022; **12**: 6606–6617.

148 Chen JW, Zhang Z, Yan HM, *et al.* Pseudo-adsorption and long-range redox coupling during oxygen reduction reaction on single atom electrocatalyst. *Nat Commun* 2022; **13**: 1734.

149 Deringer VL, Caro MA, Csányi G. Machine learning interatomic potentials as emerging tools for materials science. *Adv Mater* 2019; **31**: 1902765.

150 Jin L, Ji Y, Wang H, *et al.* First-principles materials simulation and design for alkali and alkaline metal ion batteries accelerated by machine learning. *Phys Chem Chem Phys* 2022; **23**: 21470–21483.

151 Huo J, Shen Z, Cao X, *et al*. Macro/micro-environment regulating carbon-supported single-atom catalysts for hydrogen/oxygen conversion reactions. *Small* 2022; **18**: e2202394.

152 Han SG, Ma DD, Zhu QL. Atomically structural regulations of carbon-based single-atom catalysts for electrochemical CO_2 reduction. *Small Methods* 2021; **5**: e2100102.

153 Hu XM, Hval HH, Bjerglund ET, *et al.* Selective CO_2 reduction to CO in water using earth-abundant metal and nitrogen-doped carbon electrocatalysts. *ACS Catal* 2018; **8**: 6255–6264.

154 Tang C, Chen L, Li H, *et al.* Tailoring acidic oxygen reduction selectivity on single-atom catalysts via modification of first and second coordination spheres. *J Am Chem Soc* 2021; **143**: 7819–7827.

155 Zhuo HY, Zhang X, Liang JX, *et al.* Theoretical understandings of graphene-based metal single-atom catalysts: stability and catalytic performance. *Chem Rev* 2020; **120**: 12315–12341.

156 Wang X, Chen Z, Zhao X, *et al.* Regulation of coordination number over single Co sites: Triggering the efficient electroreduction of CO_2. *Angew Chem Int Ed* 2018; **57**: 1944–1948.

157 Yuan K, Lützenkirchen-Hecht D, Li L, *et al.* Boosting oxygen reduction of single iron active sites via geometric and electronic engineering: Nitrogen and phosphorus dual coordination. *J Am Chem Soc* 2020; **142**: 2404–2412.

158 Zhang Y, Guo L, Tao L, *et al.* Defect-based single-atom electrocatalysts. *Small Methods* 2018; **3**: 1800406.

159 Pan F, Li B, Sarnello E, *et al.* Pore-edge tailoring of single-atom iron-nitrogen sites on graphene for enhanced CO_2 reduction. *ACS Catal* 2020; **10**: 10803–10811.

160 Li R, Wang D. Superiority of dual-atom catalysts in electrocatalysis: One step further than single-atom catalysts. *Adv Energy Mater* 2022; **12**: 2103564.

161 Wang J, Huang Z, Liu W, *et al.* Design of N-coordinated dual-metal sites: A stable and active Pt-free catalyst for acidic oxygen reduction reaction. *J Am Chem Soc* 2017; **139**: 17281–17284.

162 Zhu C, Fu S, Song J, *et al.* Self-assembled Fe-N-doped carbon nanotube aerogels with single-atom catalyst feature as high-efficiency oxygen reduction electrocatalysts. *Small* 2017; **13**: 1603407.

163 Liu D, Li JC, Shi Q, *et al.* Atomically isolated iron atom anchored on carbon nanotubes for oxygen reduction reaction. *ACS Appl Mater Interfaces* 2019; **11**: 39820–39826.

164 Zhang Q, Duan Z, Li M, *et al.* Atomic cobalt catalysts for the oxygen evolution reaction. *Chem Commun* 2020; **56**: 794–797.

165 Li JC, Cheng M, Li T, *et al.* Carbon nanotube-linked hollow carbon nanospheres doped with iron and nitrogen as single-atom catalysts for the oxygen reduction reaction in acidic solutions. *J Mater Chem A* 2019; **7**: 14478–14482.

166 Niu X, Shi Q, Zhu W, *et al.* Unprecedented peroxidase-mimicking activity of single-atom nanozyme with atomically dispersed Fe-N_x moieties hosted by MOF derived porous carbon. *Biosens Bioelectron* 2019; **142**: 111495.

167 Narendra Kumar AV, Muthu Prabhu S, Shin WS, *et al.* Prospects of non-noble metal single atoms embedded in two-dimensional (2D) carbon and non-carbon-based structures in electrocatalytic applications. *Coord Chem Rev* 2022; **467**: 214613.

168 Wang G, Chen J, Ding Y, *et al.* Electrocatalysis for CO_2 conversion: From fundamentals to value-added products. *Chem Soc Rev* 2021; **50**: 4993–5061.

169 Song RB, Zhu W, Fu J, *et al*. Electrode materials engineering in electrocatalytic CO_2 reduction: energy input and conversion efficiency. *Adv Mater* 2020; **32**: e1903796.

170 Tan X, Yu C, Ren Y, *et al.* Recent advances in innovative strategies for the CO_2 electroreduction reaction. *Energy Environ Sci* 2021; **14**: 765–780.

171 Lv JJ, Yin R, Zhou L, *et al*. Microenvironment engineering for the electrocatalytic CO_2 reduction reaction. *Angew Chem Int Ed* 2022; **61**: e202207252.

172 Wang G, Li X, Yang X, *et al.* Metal-based aerogels catalysts for electrocatalytic CO_2 reduction. *Chem Eur J* 2022; **28**: e202201834.

173 Du H, Fu J, Liu LX, *et al.* Recent progress in electrochemical reduction of carbon monoxide toward multi-carbon products. *Mater Today* 2022; **59**: 182–199.

174 Liu LX, Li X, Cai Y, *et al.* Hierarchical S-modified Cu porous nanoflakes for efficient CO_2 electroreduction to formate. *Nanoscale* 2022; **14**: 13679–13688.

175 Zhu W, Michalsky R, Metin Ö, *et al.* Monodisperse Au nanoparticles for selective electrocatalytic reduction of CO_2 to CO. *J Am Chem Soc* 2013; **135**: 16833–16836.

176 Zhu W, Zhang YJ, Zhang H, *et al.* Active and selective conversion of CO_2 to CO on ultrathin Au nanowires. *J Am Chem Soc* 2014; **136**: 16132–16135.

177 Liu J, Fu J, Zhou Y, *et al.* Controlled synthesis of EDTA-modified porous hollow copper microspheres for high-efficiency conversion of CO_2 to multicarbon products. *Nano Lett* 2020; **20**: 4823–4828.

178 Yi J, Xie R, Xie Z, *et al.* Highly selective CO_2 electroreduction to CH_4 by *in situ* generated Cu_2 O single-type sites on a conductive MOF: Stabilizing key intermediates with hydrogen bonding. *Angew Chem Int Ed* 2020; **59**: 23641–23648.

179 Liu LX, Zhou Y, Chang YC, *et al.* Tuning Sn_3O_4 for CO_2 reduction to formate with ultra-high current density. *Nano Energy* 2020; **77**: 105296.

180 Peng C, Luo G, Zhang J, *et al.* Double sulfur vacancies by lithium tuning enhance CO_2 electroreduction to n-propanol. *Nat Commun* 2021; **12**: 1580.

181 He W, Liberman I, Rozenberg I, *et al.* Electrochemically driven cation exchange enables the rational design of active CO_2 reduction electrocatalysts. *Angew Chem Int Ed* 2020; **59**: 8262–8269.

182 Yang F, Liang C, Yu H, *et al*. Phosphorus-doped graphene aerogel as self-supported electrocatalyst for CO_2-to-ethanol conversion. *Adv Sci* 2022; **9**: e2202006.

183 Sun Q, Jia C, Zhao Y, *et al.* Single atom-based catalysts for electrochemical CO_2 reduction. *Chin J Catal* 2022; **43**: 1547–1597.

184 Fu J, Wang Y, Liu J, *et al.* Low overpotential for electrochemically reducing CO_2 to CO on nitrogen-doped graphene quantum dots-wrapped single-crystalline gold nanoparticles. *ACS Energy Lett* 2018; **3**: 946–951.

185 Liu LX, Fu J, Jiang LP, *et al.* Highly efficient photoelectrochemical reduction of CO_2 at low applied voltage using 3D Co-Pi/$BiVO_4$/SnO_2 nanosheet array photoanodes. *ACS Appl Mater Interfaces* 2019; **11**: 26024–26031.

186 Tang T, Wang Z, Guan J. Optimizing the electrocatalytic selectivity of carbon dioxide reduction reaction by regulating the electronic structure of single-atom M-N-C materials. *Adv Funct Mater* 2022; **32**: 2111504.

187 Chen B, Li B, Tian Z, *et al.* Enhancement of mass transfer for facilitating industrial-level CO_2 electroreduction on atomic Ni-N_4 sites. *Adv Energy Mater* 2021; **11**: 2102152.

188 Han N, Ding P, He L, *et al.* Promises of main group metal-based nanostructured materials for electrochemical CO_2 reduction to formate. *Adv Energy Mater* 2019; **10**: 1902338.

189 Shang H, Wang T, Pei J, *et al.* Design of a single-atom indium$^{\delta+}$-N_4 interface for efficient electroreduction of CO_2 to formate. *Angew Chem Int Ed* 2020; **59**: 22465–22469.

190 Du H, Liu LX, Cai Y, *et al. In situ* formed N-containing copper nanoparticles: A high-performance catalyst toward carbon monoxide electroreduction to multicarbon products with high faradaic efficiency and current density. *Nanoscale* 2022; **14**: 7262–7268.

191 Han L, Song S, Liu M, *et al.* Stable and efficient single-atom Zn catalyst for CO_2 reduction to CH_4. *J Am Chem Soc* 2020; **142**: 12563–12567.

192 Yang H, Wu Y, Li G, *et al.* Scalable production of efficient single-atom copper decorated carbon membranes for CO_2

electroreduction to methanol. *J Am Chem Soc* 2019; **141**: 12717–12723.

193 Zhao K, Nie X, Wang H, *et al.* Selective electroreduction of CO_2 to acetone by single copper atoms anchored on N-doped porous carbon. *Nat Commun* 2020; **11**: 2455.

194 Kortlever R, Shen J, Schouten KJP, *et al.* Catalysts and reaction pathways for the electrochemical reduction of carbon dioxide. *J Phys Chem Lett* 2015; **6**: 4073–4082.

195 Wang J, Gao Y, Kong H, *et al.* Non-precious-metal catalysts for alkaline water electrolysis: *Operando* characterizations, theoretical calculations, and recent advances. *Chem Soc Rev* 2020; **49**: 9154–9196.

196 Zang W, Sun T, Yang T, *et al.* Efficient hydrogen evolution of oxidized Ni-N_3 defective sites for alkaline freshwater and seawater electrolysis. *Adv Mater* 2021; **33**: 2003846.

197 Xue Y, Huang B, Yi Y, *et al.* Anchoring zero valence single atoms of nickel and iron on graphdiyne for hydrogen evolution. *Nat Commun* 2018; **9**: 1460.

198 Li Z, Wang Z, Xi S, *et al.* Tuning the spin density of cobalt single-atom catalysts for efficient oxygen evolution. *ACS Nano* 2021; **15**: 7105–7113.

199 Zhang Z, Feng C, Li X, *et al. In-situ* generated high-valent iron single-atom catalyst for efficient oxygen evolution. *Nano Lett* 2021; **21**: 4795–4801.

200 Li J, Meng Y, Zhang L, *et al.* Dual-phasic carbon with Co single atoms and nanoparticles as a bifunctional oxygen electrocatalyst for rechargeable Zn-air batteries. *Adv Funct Mater* 2021; **31**: 2103360.

201 Meng Y, Li JC, Zhao SY, *et al.* Fluorination-assisted preparation of self-supporting single-atom Fe-N-doped single-wall carbon nanotube film as bifunctional oxygen electrode for rechargeable Zn-air batteries. *Appl Catal B-Environ* 2021; **294**: 120239.

202 Kulkarni A, Siahrostami S, Patel A, *et al.* Understanding catalytic activity trends in the oxygen reduction reaction. *Chem Rev* 2018; **118**: 2302–2312.

203 Shah SSA, Najam T, Bashir MS, *et al.* Single-atom catalysts for next-generation rechargeable batteries and fuel cells. *Energy Storage Mater* 2022; **45**: 301–322.

204 Wei YS, Zhang M, Zou R, *et al.* Metal-organic framework-based catalysts with single metal sites. *Chem Rev* 2020; **120**: 12089–12174.

205 Li JC, Wei Z, Liu D, *et al.* Dispersive single-atom metals anchored on functionalized nanocarbons for electrochemical reactions. *Top Curr Chem (Z)* 2019; **377**: 4.

206 Hai X, Zhao X, Guo N, *et al.* Engineering local and global structures of single Co atoms for a superior oxygen reduction reaction. *ACS Catal* 2020; **10**: 5862–5870.

207 Xu H, Xi S, Li J, *et al*. Chemical design and synthesis of superior single-atom electrocatalysts via *in situ* polymerization. *J Mater Chem A* 2020; **8**, 17683-17690.

208 Sun T, Mitchell S, Li J, *et al.* Design of local atomic environments in single-atom electrocatalysts for renewable energy conversions. *Adv Mater* 2021; **33**: 2003075.

209 Shi Q, Hwang S, Yang H, *et al.* Supported and coordinated single metal site electrocatalysts. *Mater Today* 2020; **37**: 93–111.

210 Sa YJ, Seo DJ, Woo J, *et al.* A general approach to preferential formation of active Fe-N_x sites in Fe-N/C electrocatalysts for efficient oxygen reduction reaction. *J Am Chem Soc* 2016; **138**: 15046–15056.

211 Li JC, Yang ZQ, Tang DM, *et al.* N-doped carbon nanotubes containing a high concentration of single iron atoms for efficient oxygen reduction. *NPG Asia Mater* 2018; **10**: e461.

212 Cheng N, Li JC, Liu D, *et al*. Single-atom nanozyme based on nanoengineered Fe-N-C catalyst with superior peroxidase-like activity for ultrasensitive bioassays. *Small* 2019; **15**: e1901485.

213 Li JC, Tang DM, Hou PX, *et al.* The effect of carbon support on the oxygen reduction activity and durability of single-atom iron catalysts. *MRS Commun* 2018; **8**: 1158–1166.

214 Yin P, Yao T, Wu Y, *et al.* Single cobalt atoms with precise N-coordination as superior oxygen reduction reaction catalysts. *Angew Chem Int Ed* 2016; **55**: 10800–10805.

215 Zhang H, Hwang S, Wang M, *et al.* Single atomic iron catalysts for oxygen reduction in acidic media: particle size control and thermal activation. *J Am Chem Soc* 2017; **139**: 14143–14149.

216 Liu D, Li J, Ding S, *et al.* 2D single-atom catalyst with optimized iron sites produced by thermal melting of metal-organic frameworks for oxygen reduction reaction. *Small Methods* 2020; **4**: 1900827.

217 Li JC, Xiao F, Zhong H, *et al.* Secondary-atom-assisted synthesis of single iron atoms anchored on N-doped carbon nanowires for oxygen reduction reaction. *ACS Catal* 2019; **9**: 5929–5934.

218 Ding S, Lyu Z, Fang L, *et al*. Single-atomic site catalyst with heme enzymes-like active sites for electrochemical sensing of hydrogen peroxide. *Small* 2021; **17**: e2100664.

219 Li JC, Maurya S, Kim YS, *et al.* Stabilizing single-atom iron electrocatalysts for oxygen reduction via ceria confining and trapping. *ACS Catal* 2020; **10**: 2452–2458.

220 Ding S, Lyu Z, Zhong H, *et al*. An ion-imprinting derived strategy to synthesize single-atom iron electrocatalysts for oxygen reduction. *Small* 2021; **17**: e2004454.

221 Li JC, Meng Y, Ma R, *et al.* Ionothermal-transformation strategy to synthesize hierarchically tubular porous single-iron-atom catalysts for high-performance zinc-air batteries. *ACS Appl Mater Interfaces* 2021; **13**: 58576–58584.

222 Zhang W, Xu X, Zhang C, *et al.* 3D space-confined pyrolysis of double-network aerogels containing In-Fe cyanogel and polyaniline: A new approach to hierarchically porous carbon with exclusive Fe-N_x active sites for oxygen reduction catalysis. *Small Methods* 2017; **1**: 1700167.

223 Song P, Luo M, Liu X, *et al.* Zn single atom catalyst for highly efficient oxygen reduction reaction. *Adv Funct Mater* 2017; **27**: 1700802.

224 Fei H, Dong J, Feng Y, *et al.* General synthesis and definitive structural identification of MN_4C_4 single-atom catalysts with tunable electrocatalytic activities. *Nat Catal* 2018; **1**: 63–72.

225 Li F, Han GF, Noh HJ, *et al.* Boosting oxygen reduction catalysis with abundant copper single atom active sites. *Energy Environ Sci* 2018; **11**: 2263–2269.

226 Tang C, Jiao Y, Shi B, *et al.* Coordination tunes selectivity: Two-electron oxygen reduction on high-loading molybdenum single-atom catalysts. *Angew Chem Int Ed* 2020; **59**: 9171–9176.

227 Yuan K, Sfaelou S, Qiu M, *et al.* Synergetic contribution of boron and Fe-N_x species in porous carbons toward efficient electrocatalysts for oxygen reduction reaction. *ACS Energy Lett* 2017; **3**: 252–260.

228 Li JC, Zhong H, Xu M, *et al.* Boosting the activity of Fe-N_x moieties in Fe-N-C electrocatalysts via phosphorus doping for oxygen reduction reaction. *Sci China Mater* 2020; **63**: 965–971.

229 Gong H, Wei Z, Gong Z, *et al.* Low-Coordinated Co-N-C on oxygenated graphene for efficient electrocatalytic H_2O_2 production. *Adv Funct Mater* 2021; **32**: 2106886.

230 Zhang J, Yang H, Liu B. Coordination engineering of single-atom catalysts for the oxygen reduction reaction: A review. *Adv Energy Mater* 2020; **11**: 2002473.

231 Tang C, Qiao SZ. How to explore ambient electrocatalytic nitrogen reduction reliably and insightfully. *Chem Soc Rev* 2019; **48**: 3166–3180.

232 Liu D, Chen M, Du X, *et al.* Development of electrocatalysts for efficient nitrogen reduction reaction under ambient condition. *Adv Funct Mater* 2020; **31**: 2008983.

233 Ren Y, Yu C, Tan X, *et al.* Strategies to suppress hydrogen evolution for highly selective electrocatalytic nitrogen reduction: Challenges and perspectives. *Energy Environ Sci* 2021; **14**: 1176–1193.

234 Martín AJ, Shinagawa T, Pérez-Ramírez J. Electrocatalytic reduction of nitrogen: From Haber-Bosch to ammonia artificial leaf. *Chem* 2019; **5**: 263-283.

235 Ma B, Zhao H, Li T, *et al.* Iron-group electrocatalysts for ambient nitrogen reduction reaction in aqueous media. *Nano Res* 2020; **14**: 555–569.

236 Han S, Wei X, Huang Y, *et al.* Tuning the activity and selectivity of nitrogen reduction reaction on double-atom catalysts by B doping: A density functional theory study. *Nano Energy* 2022; **99**: 107363.

237 Ying Y, Fan K, Qiao J, *et al.* Rational design of atomic site catalysts for electrocatalytic nitrogen reduction reaction:

One step closer to optimum activity and selectivity. *Electrochem Energy Rev* 2022; **5**: 6.

238 Han L, Liu X, Chen J, *et al.* Atomically dispersed molybdenum catalysts for efficient ambient nitrogen fixation. *Angew Chem Int Ed* 2019; **58**: 2321–2325.

239 Mukherjee S, Yang X, Shan W, *et al.* Atomically dispersed single Ni site catalysts for nitrogen reduction toward electrochemical ammonia synthesis using N_2 and H_2O. *Small Methods* 2020; **4**: 1900821.

240 Wang M, Liu S, Qian T, *et al.* Over 56.55% Faradaic efficiency of ambient ammonia synthesis enabled by positively shifting the reaction potential. *Nat Commun* 2019; **10**: 341.

241 Kuznetsov DA, Chen Z, Abdala PM, *et al.* Single-atom-substituted Mo_2CT_x:Fe-layered carbide for selective oxygen reduction to hydrogen peroxide: Tracking the evolution of the MXene phase. *J Am Chem Soc* 2021; **143**: 5771–5778.